ENERGY TRANSFER AND OPTICAL ANISOTROPY IN SEMICONDUCTING POLYMERS

A Thesis

Submitted to the Faculty

of

Purdue University

by

Sona N. Avetian

In Partial Fulfillment of the

Requirements for the Degree

of

Master of Science

August 2019

Purdue University

West Lafayette, Indiana

THE PURDUE UNIVERSITY GRADUATE SCHOOL
STATEMENT OF THESIS APPROVAL

Dr. Libai Huang, Chair

Department of Chemistry

Dr. Jianguo Mei

Department of Chemistry

Dr. Adam Wasserman

Department of Chemistry

Approved by:

Dr. Christine Hrycyna

Head of the Graduate Program

To my mother, my greatest inspiration.

ACKNOWLEDGMENTS

I would like to thank my advisor, Professor Libai Huang, for her expertise and advice throughout my time in her lab; she is extremely knowledgeable and has been an incredible resource. I would also like to thank my lab mates, namely Dr. Tong Zhu for not only providing me constant advice and guidance, but also for her friendship both in and out of the lab. I also would like to thank Dr. Shibin Deng, Dr. Long Yuan and Dr. Ti Wang for all their patience and assistance during my formative time in the lab. Thank you to Victoria Lumsargis and Sarath Santhakumar for your friendship and laughs, which made working in the basement 10 times more enjoyable. A thank you is owed to Aristide as well, for not only providing me samples to study but also many discussions which have contributed to my growth as a scientist.

I would also like to thank my family, beginning with my brothers: Matthew, Daniel and Luke. Thank you all for your constant love, support and invaluable advice throughout my academic career. Each one of you have been a great support for me and I am incredibly lucky to have you all has big brothers. Lastly, and most importantly, I would like to thank my mother, Suzette, for providing me with the the greatest mother, role-model and best friend anyone could ask for. Thank you for everything you have done for me, and continue to do, in encouraging me to pursue my dreams.

TABLE OF CONTENTS

Page

Page

LIST OF TABLES

LIST OF FIGURES

Figure Page

Figure Page

Figure Page

ABSTRACT

Avetian, Sona N. M.S., Purdue University, August 2019. Energy Transfer and Optical Anisotropy in Semiconducting Polymers. Major Professor: Libai Huang.

To fully optimize devices for solar energy conversion, a comprehensive understanding of how excitons migrate in materials for solar cell devices is crucial. Understanding the mechanisms behind exciton diffusion and energy transfer will enable the fabrication of highly efficient devices. However to thoroughly study exciton properties, techniques implementing high spatial (nm sizes) and temporal (fs time scales) resolution is required. Herein, we utilize transient absorption microscopy (TAM) with 50 nm spatial resolution and 200 fs temporal resolution to elucidate exciton diffusion in polymeric materials for solar energy conversion.

While organic devices are inexpensive and require simpler fabrication procedures than inorganic materials, their device efficiencies often suffer due to their semicrystalline nature, lending to short diffusion lengths which lead to trap sites and inevitably recombination. It has been demonstrated that achieving long-range exciton diffusion lengths is possible through coherence effects. Coherence can be found in an intermediate electronic coupling region where delocalization and localization compete.

To exploit coherence effects, we study polymeric systems in which polymer chains are highly aligned via simple and scalable procedures; semiconducting fibers and solution coated films. In studying the fiber, we first implement polarized photoluminesce (PL) to determine optical ansitropy. From the polarized PL and PL images, it is observed that emission intensities are largest when probing along the transition dipole

moment of the polymer. This suggests a type of Förester Resonance Energy Transfer mechanism in which excitons hop from one polymer chain to another.

Solution coated polymer films are also studied to understand exciton diffusion as a function of deposition methods. By varying the solution concentration as well as coating rate, we are able to tune the morphology of the film. We observe a strong dependence between diffusion constant and deposition parameters, with diffusion constants of *ca.* 9, 13 and 33 cm^2/s for three different films. The results obtained in this thesis are preliminary steps in an effort to elucidate energy transfer mechanisms and rates.

1. INTRODUCTION

1.1 Need for Solar Energy

In 2018 the United States hit a record high of 101.3 quadrillion British Thermal units (Btu) in energy consumption, the largest increase in nearly a decade, with fossil fuels (natural gas, coal and petroleum) accounting for 80% of energy consumption [1]. Globaly, energy consumption has grown by 2.3% in 2018, two times larger than the annual rate since 2010 [2]. Driven by demands in energy consumption across the globe, CO_2 emissions rose 1.7% in 2018, accounting for nearly 75% of anthropogenic greenhouse gas emissions [3].

Globally, electricity consumption grew 4% in 2018, attributing nearly 20% of total energy consumption to the rapid growth in electricity demands [2]. In the U.S., incorporation of wind and solar sources has contributed to the increase in energy consumption; in 2018 wind and solar consumption grew by 8% and 22% respectively [1]. The U.S. Energy Information Administration projects a 28% growth in energy consumption between 2015 to 2040, with renewables expected to be the fastest growing source [1].

Although solar energy consumption is steadily increasing, optimization of solar energy capture, conversion and storage has yet to be realized. Many research efforts in improving efficncies strive to surpass the Shockley-Queisser maximum theoretical power conversion efficiency of 33% for a single p-n junction photovoltaic (PV) cell [4]. There are several apprachoes to overcoming this barrier, such as multi-junction cells and hot-carrrier devices. However, many studies focus on ensemble properties of PV devices while a comprehensive, molecular level understanding of charge carrier

pathways is lacking at present. To fully optimize PV device efficiencies, a fundamental understanding of tuning energy transport pathways is essential.

1.2 Organic Photovoltaics

Currently, crystalline silicon (c-Si) PVs contribute the largest fraction of solar energy, comprising over 90% of PV production [5]. However, manufacturing of c-Si is costly and requires several processing steps. Organic photovoltaics (OPVs), composed of conjugated molecules or polymers with delocalized electronic states, hold the potential to produce power at a significantly lower cost than current c-Si devices. Furthermore, OPVs have gained interest due to their many appealing attributes, which include the use light-weight materials, large absorption cross-sections, high solution processing, molecular tunability, mechanical flexibility and tunable electronic properties [6]. These qualities make OPVs ideal candidates for large-scale, inexpensive ink-jet printing [7]. Despite their potential, OPV power conversion efficiencies (PCEs) struggle to compete with their inorganic counterparts (i.e. c-Si), due to their semi-crystalline nature which lends to an ambiguous understanding of fundamental charge transfer pathways.

Absorption of sunlight by an OPV generates a negatively charged electron in an excited state and in this vacancy remains a positively charged hole, or lack of an electron. The electron-hole pair is bound by a Coulombic potential, forming what is known as an exciton. To efficiently separate the electron and hole, the exciton must migrate to an interface where an offset in energy levels will enable charge separation (CS) [8]. Once separated, the charges are extracted to generate photocurrent. Typical exciton diffusion lengths (L_D) for organic materials range from 10 - 20 nm [9], which is significantly shorter than the $\sim$100 nm film thickness required for sufficient sunlight absorption. As a result, the blended bulk heterojunction (BHJ) has become a benchmark for polymer photovoltaics [10].

The BHJ OPV architecture, shown in Figure 1.1, implements various interlayers to funnel and ultimately extract charges. The active layer consists of an interpolating network of an electron donating chromophore (donor) and electron accepting molecule (acceptor). Light is absorbed by the donor, generating an exciton which diffuses to the donor/acceptor interface [11]. Due to the offset between the donor highest occupied molecular orbital (HOMO), and the acceptor lowest unoccupied molecular orbital (LUMO), the electron transfers to the acceptor molecule. The hole however, remains on the donor to form a charge transfer (CT) exciton. While it is possible for the exciton to be trapped in the CT state, sufficient delocalization enables the exciton to bypass the trap state and overcome the Coulomb potential to achieve charge separation (CS) [12], [13]. After CS is achieved, the offset in energy levels of the electron selective layer (ESL) and hole selective layer (HSL) funnel electrons and holes to their respective electrodes. While the blended morphology of the active layer in the BHJ maximizes sites at which CS can occur, domain sizes are comparable to diffusion lengths, L_D, ($\sim$ 10 nm) leaving excitons susceptible to undesired recombination and resulting in overall loss in energy conversion.

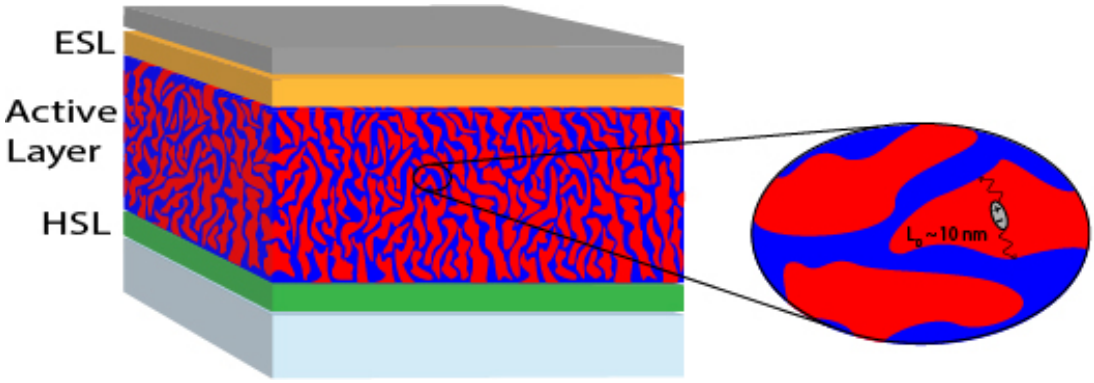

Figure 1.1. Bulk heterojunction organic photovoltaic architecture. Active layer consists of electron donating chromophore (red) and accepting material (blue). (ESL: electron-selective layer; HSL: hole-selective layer)

Achieving long-range exciton diffusion, on the order of 100 nm, will eliminate the need for complex BHJ morphologies with many small domains, instead allowing for simpler OPV designs such as incorporating larger domains which minimize recombination pathways. Such long-range exciton diffusion lengths (>200 nm) can be achieved by means of coherent energy transport, through the use of highly aligned, delocalized organic networks [14].

1.3 Frenkel Excitons

Due to the low dielectric constant of organic materials, screening of the Coulomb potential is weak, resulting in a large binding energy between electron and hole (on the order of 0.1 to 1 eV). This high Coulomb attraction creates tightly bound Frenkel excitons with small radii, such that electrons and holes reside typically on the same molecule [15]. Transport of Frenkel excitons occurs at a much slower rate and on much shorter diffusion lengths compared to inorganic Wannier excitons. Figure 1.2 provides a visual representation of a Frenkel exciton within a molecular aggregate, in which both the electron and hole reside on the same molecule.

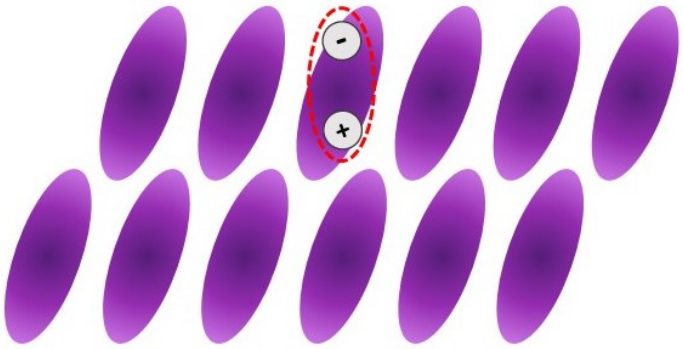

Figure 1.2. Schematic representation of a Frenkel exciton residing on one molecule within a molecular aggregate. Purple ovals depict individual molecules. Due to the high binding energy of the Frenkel exciton, both electron and hole are maintained on one molecule.

1.4 Energy Transfer

Here, energy transfer (ET) refers to the movement of an exciton from one molecule to another, wherein electron and hole both transfer. There are three mechanisms of ET: 1) Radiative ET 2) Förster Resonance ET (FRET) and 3) Dexter ET. Radiative ET entails emission from a donor followed by reabsorbed by the acceptor. While this process is prevalent in many systems, we do not directly study this as a main mode of ET. Rather, we will focus on the mechanisms of non-radiaitve ET; FRET, which occurs via dipole-dipole interactions between donor and acceptor species, and Dexter ET which occurs through wavefunction overlap. While both processes transfer an exciton, they differ greatly mechanistically as described in the following sections.

1.4.1 Förster Resonance Energy Transfer

Förster Resonance Energy Transfer (FRET) is a non-radiative transfer of an electronic excitation, occurring from a donor to an acceptor molecule through dipole-dipole coupling [16]. FRET occurs when oscillations in the optically induced excitation of the donor are resonant with oscillations in the acceptor absorption. As shown in the schematic of Figure 1.3, light is absorbed by the donor, causing an electronic excitation to the S_1 state. Following Kasha's rule, rapid relaxation occurs, leaving the excited electron in the lowest S_1 vibrational level. Weak coupling between the donor and acceptor transitions is depicted in Figure 1.3 as $\mathbf{V}$. When oscillations in the electronic transitions of both donor and acceptor are resonant (shown in Figure 1.3 red dashes), this can induce excitation of the acceptor. As a result, the donor essentially emits a "virutal photon" which is absorbed by the acceptor. It is important to note that this process does not involve emission and reabsorption of an actual photon.

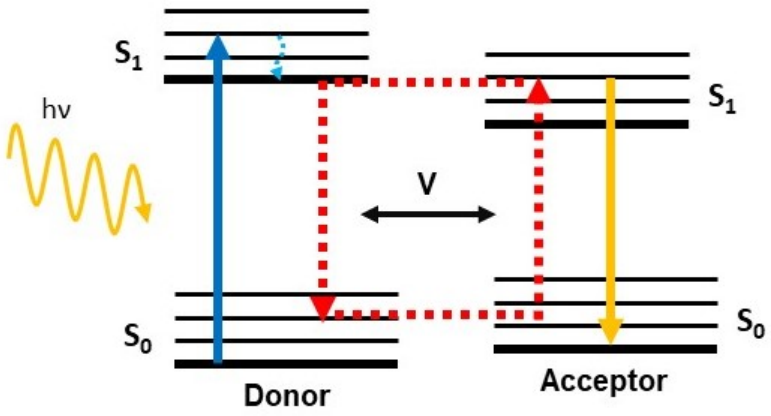

Figure 1.3. Schematic representation of FRET mechanism. Blue arrow shows absorption, red arrows illustrate the resonant energy transfer from donor, yellow arrow is acceptor emission.

Briefly, donor and acceptor species are considered as dipoles, with a partial positive charge on one end and a partial negative charge on the other end of the molecule. When molecules pack close to one another, the donor and acceptor interact in the form of a dipole-dipole interaction:

$$V = \frac{3(\overline{\mu}_{\mathrm{A}} \cdot \hat{r})(\overline{\mu}_{\mathrm{D}} \cdot \hat{r}) - \overline{\mu}_{\mathrm{A}} \cdot \overline{\mu}_{\mathrm{D}}}{\overline{r}^3} \tag{1.1}$$

Where r is the distance between donor and acceptor, $\hat{r}$ is the unit vector describing the orientation between molecules, $\overline{\mu}_{\mathrm{A}}$ and $\overline{\mu}_{\mathrm{D}}$ are the acceptor and donor dipole operators, respectively. To measure the strength of interaction causing transitions from one energy level to another within a molecule (i.e. $\psi_1 \rightarrow \psi_{\mathrm{N}}$), the transition dipole moment (TDM) is considered:

$$\overrightarrow{\mu} = \int \psi^*{}_2 \cdot e\overrightarrow{r}\psi_1 dV \tag{1.2}$$

Equation 1.2 is a complex vector, which can be considered as the off-diagonal matrix elements of the operator. This integral describes how interaction with light will cause a transition between two electronic states. The direction of the vector

provides the polarization of the transition, indicating how the molecule will interact with light of a specific polarization. The magnitude describes the strength of the transition. Thus, the dipole-dipole interaction between donor and acceptor depends on the magnitude of the donor and acceptor TDM, as well as their spatial orientation. The orientation factor, $\langle\kappa^2\rangle$, gives a quantitative value of the interaction between two dipole moments based on their position relative to each other. For instance, $\langle\kappa^2\rangle$ can range from 0 when dipoles are perpendicular, to 4 when colinear. For the dynamic, isotropic loss of orientation in donor and acceptor, the average orientation factor is considered as 2/3.

The rate of energy transfer from donor to acceptor, $\mathrm{E_{ET}}$, can be expressed by considering all relaxation pathways possible per donor excitation:

$$E_{\mathrm{ET}} = \frac{k_{\mathrm{ET}}}{k_{\mathrm{ET}} + k_{\mathrm{r}} + \sum k_{\mathrm{nr}}} \tag{1.3}$$

Where k_{ET} is the rate of FRET, k_{r} is the rate of radiative decay and k_{nr} is the rate for all non-radiative relaxation pathways (i.e. internal conversion, intersystem crossing). By implementing a dipole-dipole approximation and perturbation theory, the FRET transfer efficiency yields a $1/\mathrm{r}^6$ distance dependence, given by:

$$E_{\mathrm{ET}} = \frac{1}{1 + (\frac{r}{R_0})^6} \tag{1.4}$$

Where r is the distance between donor and acceptor and R_0 is the Förster distance, at which point the ET efficiency is 50%. The Förster distance is defined as:

$${R_0}^6 = \frac{2.07\kappa^2\phi_{\mathrm{D}}}{128\pi^5 N_{\mathrm{A}} n^4} \int J_{\mathrm{DA}} \tag{1.5}$$

Where κ is the dipole orientation factor, ϕ_D is the donor quantum yield, N_A is Avogadro's number and n is the refractive index. Furthermore, R_0 depends on the overlap integral, J_{DA}, which describes the spectral overlap between donor emission and acceptor absorption:

$$J_{\mathrm{DA}} = \int F_{\mathrm{D}}(\lambda)\epsilon_{\mathrm{A}}(\lambda)\lambda^4 d\lambda \tag{1.6}$$

Where F_D is the noramlized donor emission spectrum and ϵ_A is the acceptor extinction coefficient. This overlap integral, J_{DA}, is a measure of resonance between the donor emission and acceptor absorption.

1.4.2 Dexter Energy Transfer

In Dexter energy transfer, an exchange of electrons (and holes) occurs between an excited state donor, D*, and a ground state acceptor, A. Figure 1.4 demonstrates this two-step mechanism: the excited electron in the donor transfers to the acceptor, and the ground state electron of the acceptor transfers to the donor. For Dexter ET, spectral overlap is required similar to FRET, however an overlap of wavefunctions is also required [17]. This requires the electrons to occupy the same orbital space for the exchange to occur, meaning Dexter ET between a donor and acceptor molecule occurs within several $\mathring{A}$.

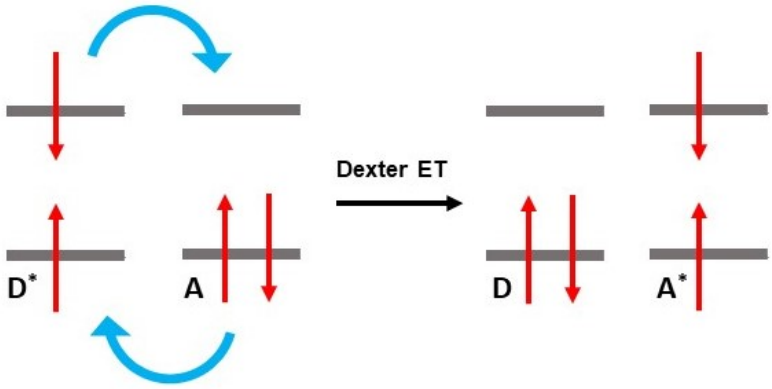

Figure 1.4. Schematic of Dexter ET: an electron (and hole) transfer from the excited state donor (D^*) and an electron (and hole) transfer from the ground state acceptor (A).

Due to the requirement of orbital overlap, the rate of Dexter ET scales exponentially with distance given by the equation:

$$k_{\mathrm{ET}} = Jexp(\frac{-2r}{L}) \tag{1.7}$$

Where J is the spectral overlap integral, r is the distance between donor and acceptor and L is the sum of Van der Waals radii of donor and acceptor.

1.5 Exciton Transport

As previously discussed, BHJ OPVs operate on the basis of excitons migrating to a D/A interface where they are able to achieve CS. Therefore, understanding the underlying mechanisms of exciton transport and energy transfer are crucial in optimizing device efficiencies. Exciton transport or energy transfer (i.e. transfer of both an electron and hole) in polymer chains can occur either by interchain (between polymer chains) or intrachain (along a polymer chain) transport [18]. This mechanism is highly dependent upon the molecular packing of polymer chains. Furthermore, both inter- and intrachain transport can propagate by either coherent or incoherent means; coherence in this regard refers to phase relations between a superposition of waves (i.e. wave-like propagation among states with amplitudes in phase) and incoherent transport occurs through a random hop between sites. It has been demonstrated that long-range exciton transport can be achieved, even in disordered systems, through coherence effects [14].

1.5.1 Incoherent vs Coherent Transport

The delocalized electronic nature of conjugated molecular and polymeric systems allows for interactions which yield unique optical and electronic properties. Weak electronic coupling between molecules leads to localized states. Transport in such systems occurs primarily through a random hopping mechanism from site to site in an incoherent manner. For instance, FRET is a form of incoherent hopping between

localized states. In contrast, when states are delocalized across various sites, energy transfer occurs in a wave-like relaxation [19]. It has been demonstrated that in highly delocalized molecular aggregates, excitons are able to migrate rapidly due to coherence among states allowing for excitons to jump larger distances in much shorter time spans [20]. Herein, coherence refers to the retention of phase relations among a superposition of waves, such that the amplitudes of states are connected and waves flow synchronously [21]. To have long-range exciton diffusion lengths enhanced by coherence, a balance between delocalized and localized states must be achieved: when there is a large degree of delocalization among molecular aggregates, the distance between donor and acceptor in the dipole-dipole approximation increases, decreasing the electronic coupling.

Diffusion lengths are determined by energy transfer hops of excitons as well as the lifetime of the excited state. The energy transfer hops typically follow a random walk pattern, in which the probability of the exciton jumping forwards is equal to jumping backwards. While both the random walk distance and lifetimes can be long (upwards of 1 nm and 1 ns) the random walk trajectory has no direction and thus the overall distance the exciton travels is minimal (*ca.* 10-30 nm). Thus, to achieve desired long-range transport excitons must migrate long distances within a short time. An intermediate regime between localized and delocalized states, which facilitates fewer exciton hops occurring over larger distances, can simplify the random walk trajectory and increase exciton diffusion lengths [22]. As a result, the intermediate coupling regime–where delcoalization and localization compete–offers the basis for long-range energy transfer mechanisms [23]. However at present, a thorough understanding of these mechanisms remains largely ambiguous.

2. OPTICAL ANALYSIS TECHNIQUES

2.1 Steady-State and Time-Resolved Photoluminescence

All steady-state and time-resolved photoluminescence (PL) spectra are collected utilizing a home-built, con-focal PL laser setup, illustrated in Figure 2.1. The setup employs a pico-second pulsed laser diode (Pico-Quant, LDH-P-C-450B) with a fixed wavelength of 447 nm, full-width half-max (FWHM) of 50 ps and repetition frequency of 40 MHz. The beam is focused using a 40× objective to excite the sample, and the emission is collected through the same objective and directed to a monochromator (Andor Technology) followed by detection via a charge coupled device (CCD) (Andor Technology). PL lifetimes are measured using a single photon avalanche diode (Pico-Quant, PDM series), with time resolution of ∼100 ps.

To measure polarized PL and TR-PL, a half-wave plate and thin film polarizer are utilized in the aforementioned PL system. A half-wave plate ($\lambda/2$) is placed before the sample, as shown in Figure 2.1. The $\lambda/2$ wave plate linearly polarizes the light, such that the beam intensity is maintained. In the collection path from the sample, a thin-film polarizer is implemented, which filters out light of a particular polarization. This allows for only emitted light corresponding to a desired linear polarization direction to be detected.

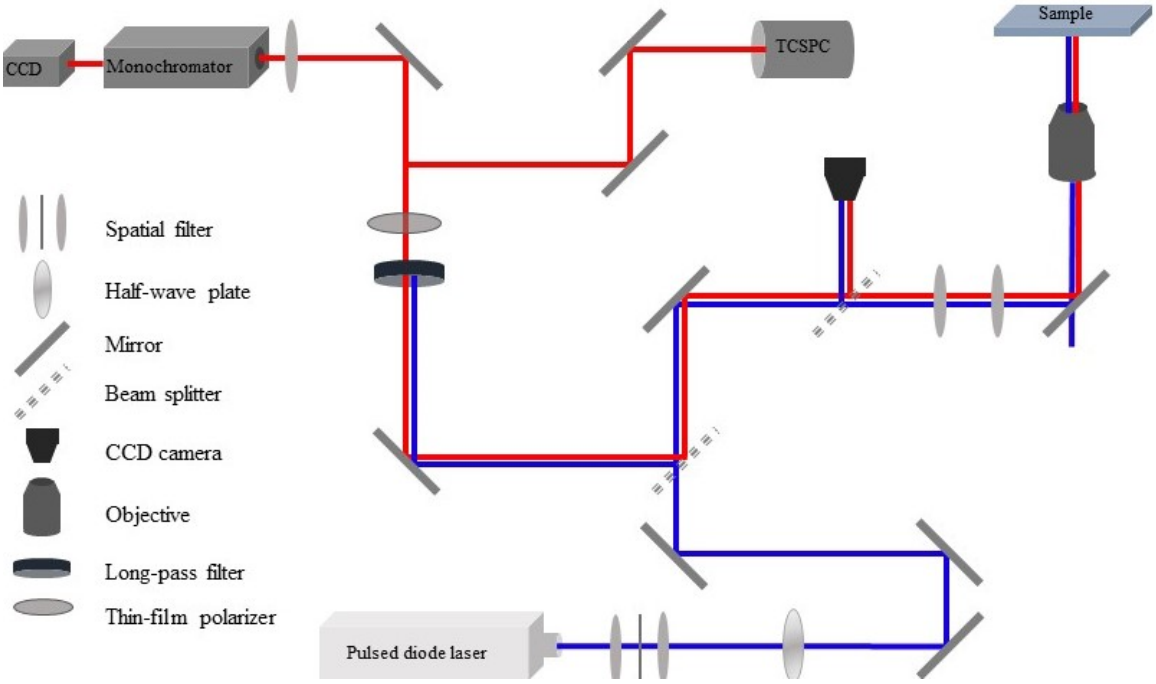

Figure 2.1. A schematic of the PL setup implemented with a fixed 447 nm pulsed laser diode. The $\lambda/2$ plate and thin-film polarizer are utilized for polarized PL measurements only. (CCD - Charge coupled device; TCSPC-time-correlated single-photon counting)

2.2 Transient Absorption Spectroscopy

The transient absorption spectroscopy (TAS) system employs a high repetition rate ultra-fast amplifier system (Light Conversion Pharos), which is tunable from 1-400 KHz. Output of the fundamental laser is divided into pump and probe beams; an optical parametric amplifier (OPA) generates ∼200 fs pulses tunable from 315-2000 nm for the pump, while the probe beam passes through a 2 mm thick YAG crystal to obtain a white light continuum. The pump beam is modulated, using a mechanical chopper, at 100 Hz. As shown in the block representation of Figure 2.2, the pump and probe colinear beams are focused using a 15× reflective microscope objective to

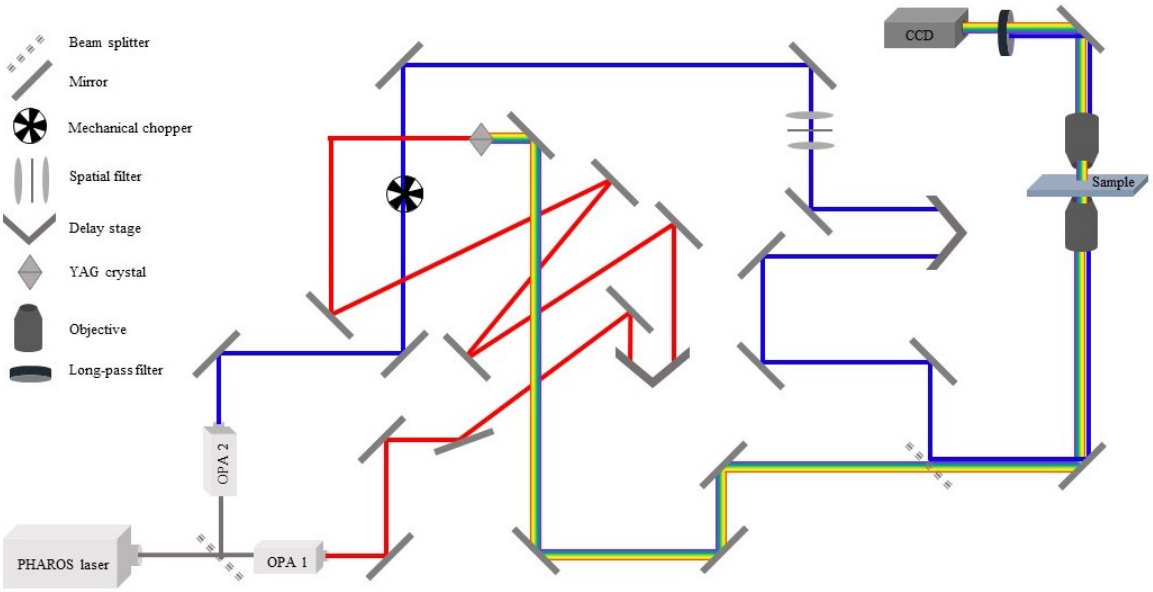

Figure 2.2. Schematic of the transient absorption spectroscopy system. The 1030 nm base probe beam (red) is converted to a white light probe source using the YAG (Yttrium aluminium garnet) crystal. (OPA-Optical parametric amplifier; CCD-Charge coupled device)

correct for chromatic aberrations. After the sample, the beams are collected using a 20× objective and focused onto a fiber optic cable connected to a CCD detector.

2.3 Transient Absorption Microscopy

The transient absorption microscopy (TAM) images are obtained through a home-built system, shown in the schematic representation of Figure 2.3. The high-repetition rate, ultra-fast amplifier laser system (Light Conversion Pharos) has a repetition rate which is tunable from 1-400 kHz. The fundamental beam intersects a beam splitter, which directs to two independent optical parametric amplifiers (OPAs) (Light Conversion), which provide ∼200 fs pulses ranging from 315-2000 nm; this allows for direct control over the pump and probe wavelengths. The probe beam intersects a

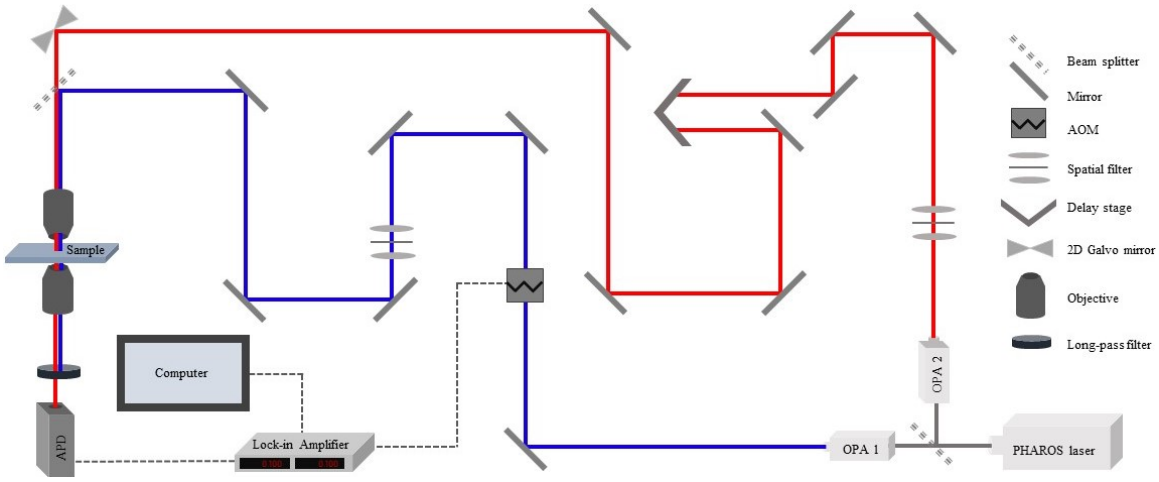

Figure 2.3. Schematic of the transient absorption microscopy system. Two OPAs allow for tuning both pump and probe wavelengths. Lock-in amplifier sets pump frequency to reference to detect small ($\sim 10^{-7}$) signal intensities. (OPA-Optical parametric amplifier; APD-Avalanche photodiode detector)

two-axis galvanometer scanning mirror, which enables control in positioning pump and probe beams relative to one another. Furthermore, this allows for scanning the probe beam–while fixing the pump beam–to capture the carrier population position generated by the pump at varying time delays. Time delays between pump and probe are controlled by an optical delay stage, which extends the optical path length of the probe and is capable of scanning pump-probe delays from 6 fs to 8 ns. Both pump and probe beams are combined colinearly to a 60× objective and focused on the sample. The beams are then collected by an inverted, high numerical aperture (NA = 1.49) objective, which directs the beams to an avalanche photodiode detector (APD). An acousto-optic modulator (AOM) is implemented to modulate the 400kHz pump beam by half, to 200 kHz. The APD detects absorbance signals relative to the reference, which is set by the lock-in amplifier. The lock-in amplifier reference is set to the modulated pump frequency. Therefore, changes in the probe absorbance

(ΔA), induced by the pump frequency, are detected by the lock-in. Due to the high sensitivity of the lock-in, our TAM system is capable of detecting induced pump signals even at very low intensities (ΔA signal as low as 10^{-7}).

At delay time 0 ps and initial position (x_0, y_0), the pump beam excites an initial population, n(x_t, y_t, 0). For any given delay time, t, the population can be expressed as n(x, y, t). The carrier population, n(x_t, y_t, 0), is given by:

$$n(x,y,0) = Nexp(-\frac{(x-x_0)^2}{2\sigma^2{}_{x,0}} - \frac{(y-y_0)^2}{2\sigma^2{}_{y,0}}) \tag{2.1}$$

Equation 2.1 describes the initial population created by the pump beam, which follows a Gaussian distribution. The diffusion of the generated excitons can be described by the differential equation:

$$\frac{\partial n(x,y,t)}{\partial t} = D(\frac{\partial n^2(x,y,t)}{\partial x^2} + \frac{\partial n^2(x,y,t)}{\partial y^2}) - \frac{n(x,y,t)}{\tau} \tag{2.2}$$

Where D is the diffusion constant and τ is the exciton lifetime. The solution to equation 2.2 describes the population distribution at a later time, t, which is also Gaussian:

$$n(x,y,t) = Nexp(-\frac{(x-x_0)^2}{2\sigma^2{}_{x,\,t}} - \frac{(y-y_0)^2}{2\sigma^2{}_{y,\,t}}) \tag{2.3}$$

The variance in both x and y, $\sigma^2{}_{x,\,t}$ and $\sigma^2{}_{y,\,t}$, are defiend as:

$$\sigma^2{}_{x,\,t} = \sigma^2{}_{x,\,0} + 2D_x t \tag{2.4}$$

$$\sigma^2{}_{y,\,t} = \sigma^2{}_{y,\,0} + 2D_y t \tag{2.5}$$

The exciton transport length, $L_{x(y)}$, is proportional to the difference in the varaince of the carrier profiles, moreover:

$$L^2{}_{x(y)} = \sigma^2{}_{x(y),\,t} - \sigma^2{}_{x(y),\,0} = 2D_{x(y)}t \tag{2.6}$$

Therefore the diffusion constant, $D_{x(y)}$ can be extracted, providing:

$$D_{\mathrm{x(y)}} = \frac{{\sigma^2}_{\mathrm{x(y),\,t}} - {\sigma^2}_{\mathrm{x(y),\,0}}}{2t} \tag{2.7}$$

In measuring the variance of the generated carrier distribution, the pump and probe and probe beam profiles are convoluted, such that

$$\sigma^2(measured) = \sigma^2(carriers) + \sigma^2(pump) + \sigma^2(probe) \tag{2.8}$$

As both pump and probe beams are collimated their variance will not change, meaning $\sigma^2(pump)$ and $\sigma^2(probe)$ are constant in time. Therefore, any changes in the variance are attributed directly to carrier population profiles, $\sigma^2(carriers)$. This technique enables a direct measurement of carrier population diffusion.

3. OPTICAL PROPERTIES OF POLYMER MICROFIBERS

3.1 Introduction

Devices constructed from semiconducting polymers are often processed from solutions, allowing for versatile deposition techniques and methods. Though organic devices are typically fabricated in the form of thin films, polymer micro and nanofibers have received great interest due to their large surface area to volume ratio, flexibility in surface functionalities and mechanical performance (i.e. tensile strength) [24]. These appealing attributes make semiconducting polymer fibers suitable for applications in flexible and stretchable electronic devices [25].

Several processing techniques are used to synthesize polymer fibers, such as drawing, template synthesis, phase separation, self-assembly and electrospinning. Currently, electrospinning of polymer fibers is widely implemented, however these fabrication techniques are not conducive to semiconducting polymers. Due to the limited solubility and tendency of aggregation [26], semiconducting polymers are often blended with insulating polymers for electrospinning, which substantially decreases electronic properties (i.e. transport) compared to pure semiconducting materials [27]. Furthermore, melt-drawing of pure semiconducting polymers is often difficult to achieve due to high temperatures which often lead to decomposition. Recently, a method to create polymer fibers from developed complimentary semiconducting polymer blends (c-SPBs), which incorporate conjugation-break spacers (CBSs) along the backbone of a fully conjugated polymer, has been demonstrated [28], [29]. Introduction of the CBS in the molecular design of this polymer enables melt-processing at high tem-

peratures (∼180 °C), while limiting macroscopic phase separation often induced by insulating/semiconducting polymer blends [30].

Microfibers are pulled from a melted solution of polymer chains, offering a simple and scalable method to produce highly aligned fibers for use in light-weight and flexible devices. As fibers are drawn from a melted solution, this removes the use of toxic solvents and their associated solvation effects. While it has been demonstrated that these highly mechanically flexible fibers exhibit anisotropic optical and electronic properties, the underlying exciton transport mechanism remains ambiguous [30]. Herein, we explore the optical anistropy of melt-drawn polymer microfibers to elucidate how energy transports among highly ordered polymer chains.

3.2 Sample Preparation and Characterization

Details on the fiber fabrication process is described elsewhere [30]. In an N_2 glove-box, solid DPP-C5 (see Figure 3.1 for structure) is heated on a glass substrate at ca. 170 °C. Once liquid, a needle is inserted into the solution to draw the polymer out and pulled at a continuous speed (∼50 cm/s). While pulling, the fiber is pressed against a glass cover slip (15 mm thick). The pressed fiber is sealed between two glass cover slips using an epoxy adhesive in an N_2 glove-box.

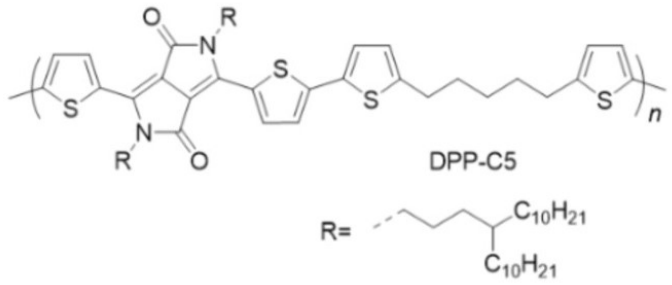

Figure 3.1. Molecular structure of DPP-C5 used to construct polymer microfibers.

The absorption and emission spectra of the polymer fiber are shown in Figure 3.2. The emission spectrum of the fiber is Stoke's shifted from the absorbance (maximum absorbance intensity at 600 nm) by 120 nm (maximum emission at 820 nm). Spectral overlap of the emission and absorbance occurs from ∼650-900 nm.

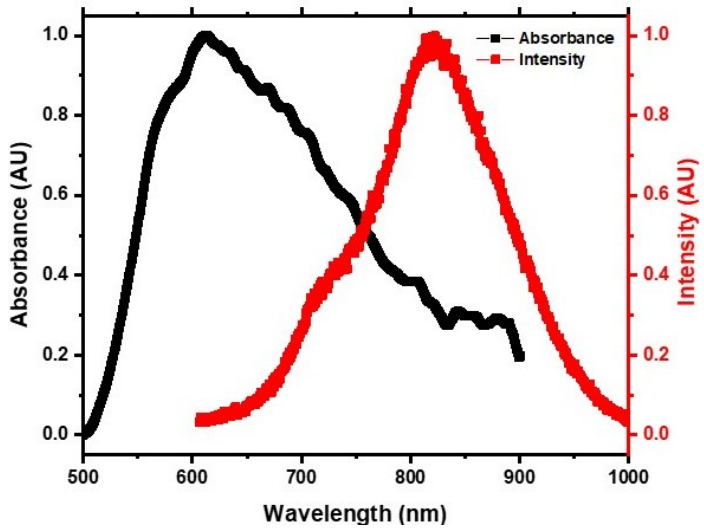

Figure 3.2. Absorbance and PL emission spectra for melt-drawn polymer fibers. Absorption maximum at *ca.* 600 nm, emission maximum at *ca.* 820 nm.

3.3 Results and Discussion

3.3.1 Optical Anisotropy

Cross polarized optical microscopy (C-POM) images from a fluorescence microscope are shown in Figure 3.3. The orientation of the cross polarization is indicated by the cross hairs on the top-left of the image. Cross-polarization is achieved by implementing two polarizers: the first polarizer linearly polarizers light incident on the sample, while the second polarizer is orthogonal to the first and polarizes the collected light. Small domains along the length of the fiber are observed, varying in shape and size. Upon rotating the sample, total light extinction is observed when

the long axis of the fiber aligns with either axis of the polarized light, as seen in the right panel of Figure 3.3. When the sample is oriented 45° from either polarizer (shown in the left panel of 3.3), the domains appear bright. This observed optical anisotropy is due to polymer chain alignment in the fiber, either perpendicular or parallel to the fiber's long axis. If the polymer chains were amorphous, or maintained no preferential orientation, rotating the fiber in the cross-polarized light would not change the optical properties. This is in good agreement with long-range ordering observed from melt-drawing of similar fibers, demonstrating a high degree of control in chain alignment.

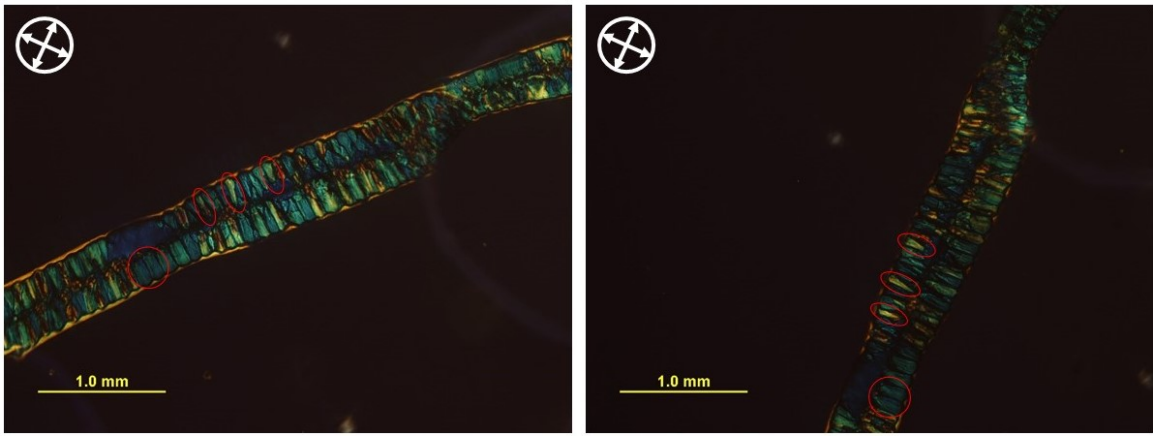

Figure 3.3. Cross-polarized optical microscope (c-POM) images of a polymer microfiber. The white cross-hairs indicate the cross-polarization axis. The left panel shows the fiber out of either cross-polarization axis, whereas the right panel shows the fiber aligned with the cross-polarization. Total light extinction is observed in the right panel, when the fiber is rotated in the polarization direction. The red circles indicate domains that are further analyzed, from left to right: domain 1, 2, 3, 4, and 5.

3.3.2 Polarized PL and TR-PL

PL spectra along the length of the fiber, at varying locations, are also collected, ensuring that the PL shape does not change significantly between locations throughout the fiber. This demonstrates that although domains within the fiber possesses a relatively large degree of inhomogeneity (in morphology and thickness), emission spectra are consistent and comparable not only throughout a domain, but also among different domains.

As mentioned previously, polarized PL is implemented to probe the orientation of polymer chains within the fiber. The $\lambda/2$ plate is used to polarize the excitation beam either along the polymer long axis (excitation parallel, $\parallel$) or along the polymer short axis (excitation perpendicular, $\perp$). The thin film polarizer then collects emitted light, again either along the polymer long axis (parallel, $\parallel$) or short axis (perpendicular, $\perp$).

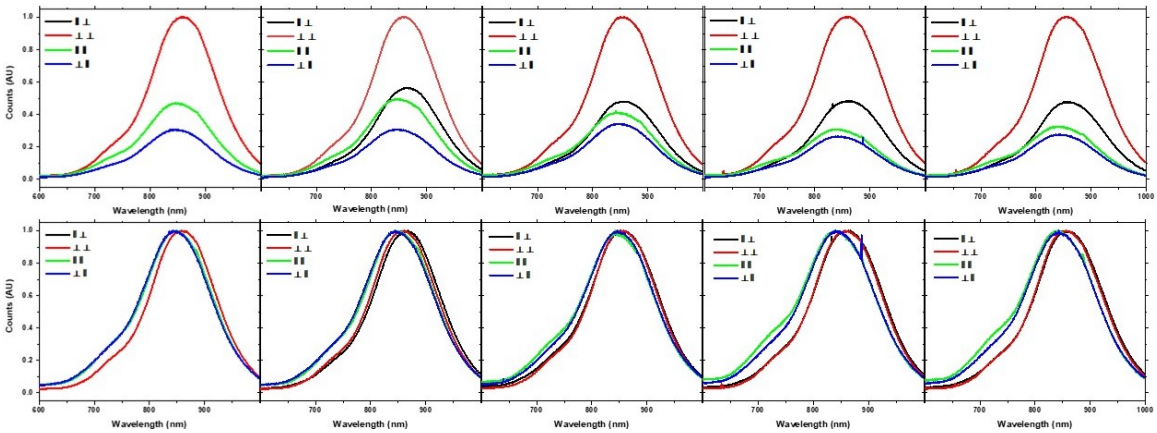

Figure 3.4. Polarized PL spectra of fiber 1, from left to right: domain 1, 2, 3, 4, and 5. Top panel has spectra normalized to the max PL intensity, showing relative differences in intensities with polarization direction. Bottom panel has spectra normalized to 1, demonstrating there is no significant change in spectral line shape with changing polarization direction.

Polarized PL spectra for five different domains on one fiber (fiber 1) are shown in Figure 3.4. The first set of spectra show all polarization configurations, normalized to the maximum intensity. It can be seen that in all polarization directions, the maximum PL intensity corresponds to perpendicular excitation and detection ($\perp$, $\perp$). For DPP based polymers, the TDM lies along the backbone of the polymer [31]. This indicates that the TDM of polymer chains, in all domains, are aligned along the short axis of the fiber. As the TDM corresponds to the electronic transition from one state to another, exciting (and detecting) in this direction provides the highest PL intensity arising from radiative relaxation from the excited state, observed in the polarized PL spectra. Included in Figure 3.4 is the same polarized PL spectra normalized to (0, 1). From this, it is observed that the line shape of the PL spectra does not change significantly, with only a slight red-shift of the PL peak when detecting perpendicularly. This confirms consistency between varying polarization directions, further illustrating that changes in PL intensity are attributed to probing along, or orthogonal, to the TDM.

Power dependent TR-PL is collected to ensure there is no dependence on pump fluence, arising from processes such as exciton-exciton annihilation, where two excitons combine to form one exciton of higher energy [32]. Time-resolved excitation lifetimes, at varying pump power, are fit with a bi-exponential decay convoluted with the laser pump; the corresponding lifetimes are provided in Table 3.1. From fitting, two lifetimes are extracted, τ_1 and τ_2. Varying pump power does not significantly change τ_1 or τ_2, demonstrating no power dependence within microfibers.

Table 3.1.
Power-Dependent TR-PL Lifetimes of Polymer Microfibers

Power (μW)	τ_1 (ps)	τ_2 (ps)
11	18.23	68.85
3	20.11	71.84
1	16.72	63.38
0.7	16.62	58.83
0.13	13.31	47.40

Polarized TR-PL is conducted on domains 1 and 3 of fiber 1, with the same polarization configurations as the polarized PL, as shown in Figure 3.5. Again fitting with a convoluted bi-exponential, lifetimes are extracted and provided in Table 3.2. It is observed that both lifetimes, τ_1 and τ_2, do not change significantly with polarization. TR-PL measures how long an electron remains in the excited state, suggesting that the rate for radiative recombination pathways do not exhibit a polarization dependence. While two distinct lifetimes are identified, these are representative of numerous pathways in which the exciton returns to the ground state from the excited state. As a result of TR-PL measuring a plethora of pathways, it is difficult to observe a polarization dependence in TR-PL lifetimes depending upon the morphology of the domain.

Table 3.2.
Polarized TR-PL Excited State Lifetimes for Fiber 1: Domains 1 and 3.

Domain	Excitation	Detection	τ_1 (ps)	τ_1 (ps)
1	∥	∥	57	246
	∥	⊥	48	211
	⊥	⊥	51	228
	⊥	∥	48	211
3	∥	∥	55	237
	∥	⊥	54	226
	⊥	⊥	62	234
	⊥	∥	44	205

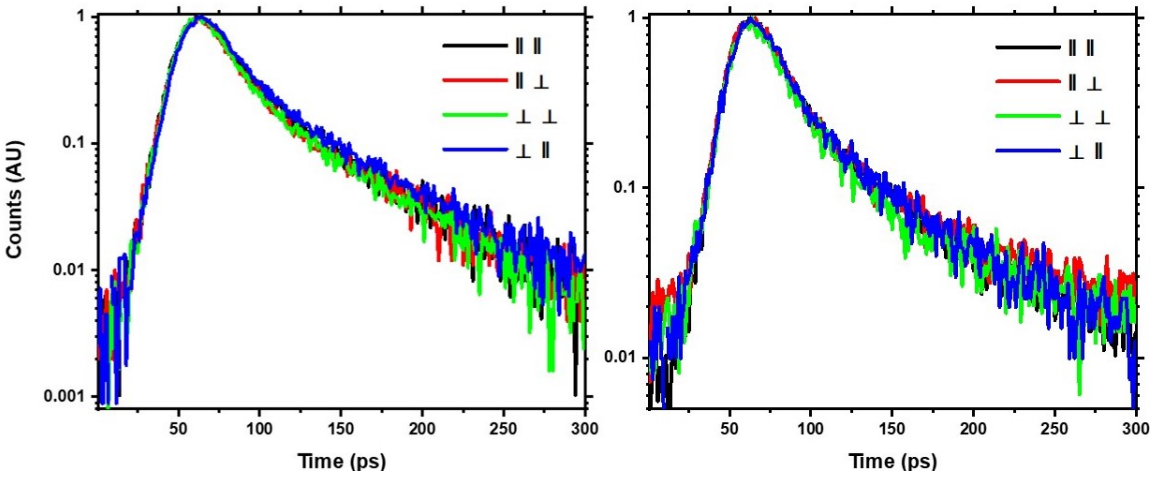

Figure 3.5. Polarized TR-PL of domains 1 (left) and 3 (right) of fiber 1, for all polarized excitation and detection directions. Excited state lifetimes are similar for all polarization configurations, suggesting lifetimes for both domains exhibit no polarization dependence. Corresponding lifetimes are found in Table 3.2.

Another polymer microfiber (fiber 2) is studied under polarized TR-PL, for three various domains. The associated excited state lifetime decays are provided in Figure 3.6, where domains 1, 2 and 3 correspond to the spectra from left to right. The first two domains, 1 and 2, do not exhibit any polarization dependence, however it is observed that domain 3 excited state lifetimes vary with polarization configurations. Parallel excitation, parallel detection ($\parallel$, $\parallel$) and perpendicular excitation, parallel detection ($\perp$, $\parallel$) polarizations yield τ_1 excited state lifetimes of 78 ps and 81 ps, respectively, values similar to other domains. This agrees with the polarized PL, in which the $\parallel$, $\parallel$ and $\perp$, $\parallel$ spectra provide the lowest PL intensities. The remaining polarizations, $\parallel$, $\perp$ and $\perp$, $\perp$, which have the highest polarized PL intensities, also exhibit significantly longer lifetimes. This is in agreement with a FRET mechanism occurring along the short axis of the fiber, in the direction of the TDM; probing perpendicular to the long axis of the fiber, along the TDM of the polymer, increases both excited state lifetimes τ_1 and τ_2 due to ET between polymer chains, extending the exciton lifetime.

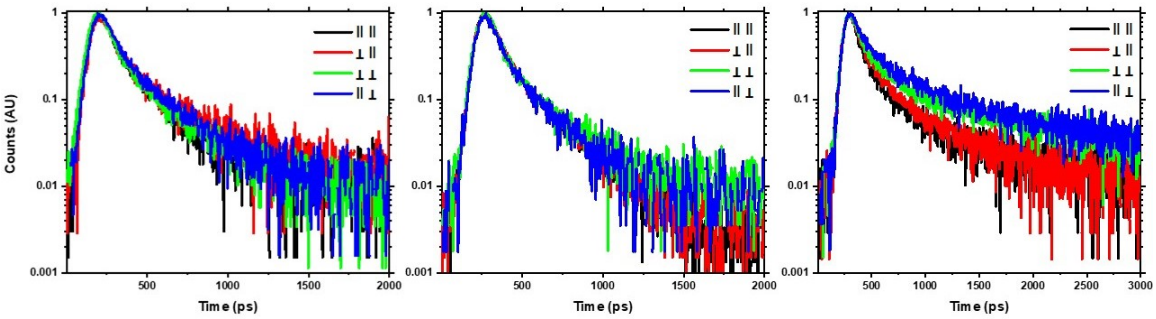

Figure 3.6. Polarized TR-PL of domains (from left to right) 1, 2 and 3 of fiber 2. Varying the excitation and detection polarization does not impact excited state lifetimes for domain 1 and 2, however domain 3 exhibits a high polarization dependence. Corresponding lifetimes are found in Table 3.3.

Table 3.3.
Polarized Excited State Lifetimes for Fiber 2: Domains 1, 2 and 3.

Domain	Excitation	Detection	τ_1 (ps)	τ_1 (ps)
1	$\parallel$	$\parallel$	52	264
	$\parallel$	$\perp$	64	311
	$\perp$	$\perp$	70	336
	$\perp$	$\parallel$	78	442
2	$\parallel$	$\parallel$	85	250
	$\parallel$	$\perp$	55	222
	$\perp$	$\perp$	46	263
	$\perp$	$\parallel$	58	245
3	$\parallel$	$\parallel$	78	635
	$\parallel$	$\perp$	133	1293
	$\perp$	$\perp$	106	1181
	$\perp$	$\parallel$	81	483

3.3.3 Polarized PL Imaging

PL imaging is achieved by utilizing the TCSPC in conjunction with piezo-electric galvo mirrors, which incrementally step the beam to provide a topographical image mapping PL intensity. For fiber 1, polarized PL images are obtained for domains 1-5, shown in Figure 3.7. The excitation and detection direction relative to the fiber long axis are indicated as follows from left to right: parallel excitation, parallel detection; parallel excitation, perpendicular detection; perpendicular excitation, parallel detection; perpendicular excitation, perpendicular detection. The PL intensities of the images are in good agreement with the PL spectra, meaning the perpendicular excitation and detection ($\perp$, $\perp$) provides the highest PL intensity spectra as well as highest PL intensity image. PL images illustrate the majority of polymer chain back-

bones, along which is the TDM, lay along the fiber short axis. From these images, it is clear that within the domains there is a high degree of optical anisotropy, while the edge of the fiber does not display any polarization dependencies.

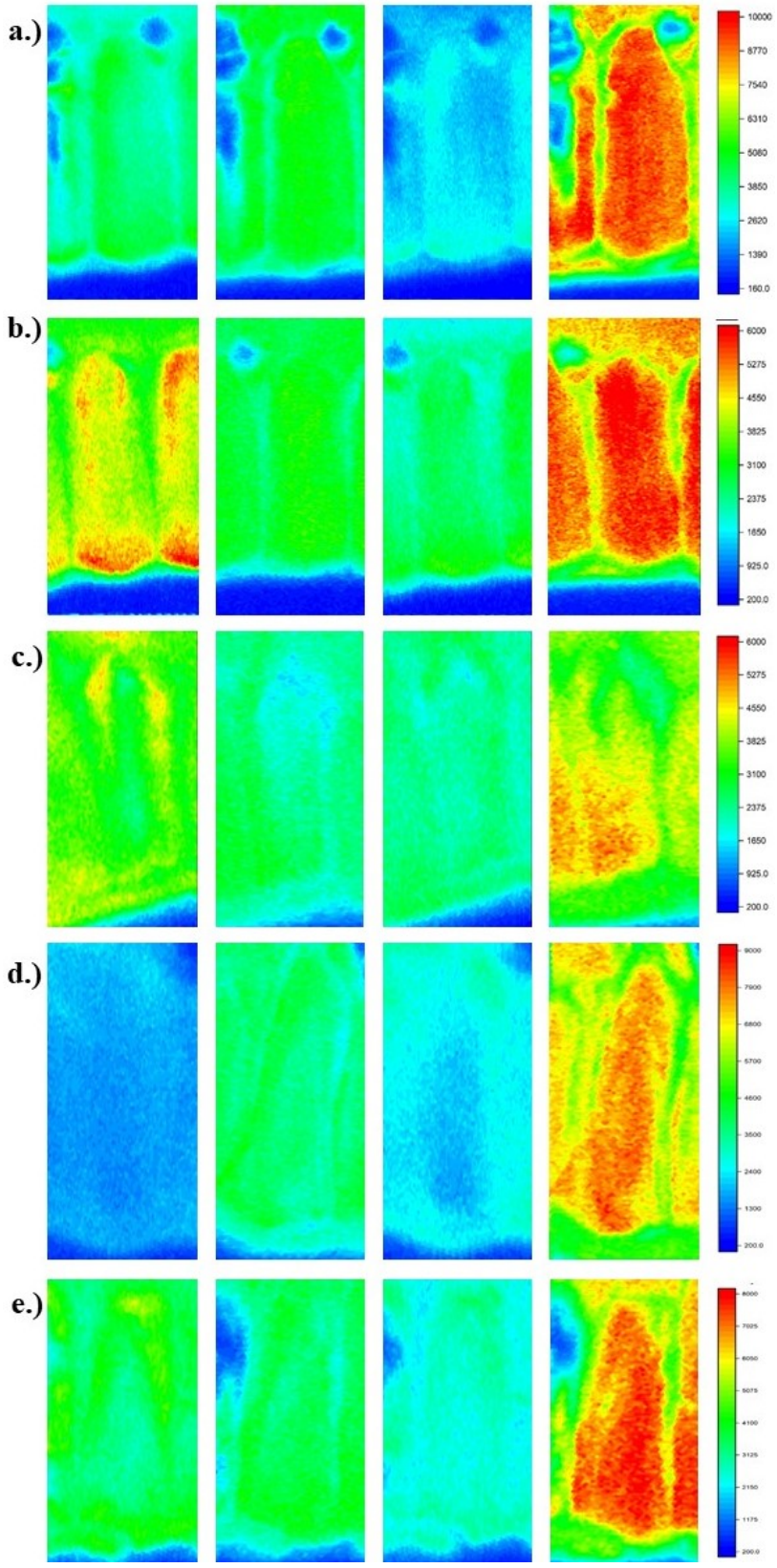

Figure 3.7. Polarized PL images of fiber 1, for domains a) 1 b) 2 c) 3 d) 4 e) 5. With (excitation, detection) directions from left to right: ($\parallel$, $\parallel$), ($\parallel$, $\perp$), ($\perp$, $\parallel$), ($\perp$, $\perp$).

3.3.4 Transient Absorption Spectroscopy

Transient absorption spectroscopy (TAS) is conducted on both fibers (1 and 2), to elucidate non-radiative recombination pathways. Figure 3.8 shows TA spectra with pump wavelength of 400 nm and a white light probe at several time delays, which includes kinetics at the 720 nm signal. From the TA spectra (Figure 3.8 a), the ground state bleach (GSB) is observed at *ca.* 700 nm while the photo-induced absorption (PIA) is positioned at *ca.* 850 nm. The normalized GSB (Figure 3.8 b) and PIA (Figure 3.8 c) kinetics are provided as well for the first 400 ps, while the inset shows the first 100 ps. Lifetimes of the GSB and PIA nearly completely decay within the first *ca.* 100 ps.

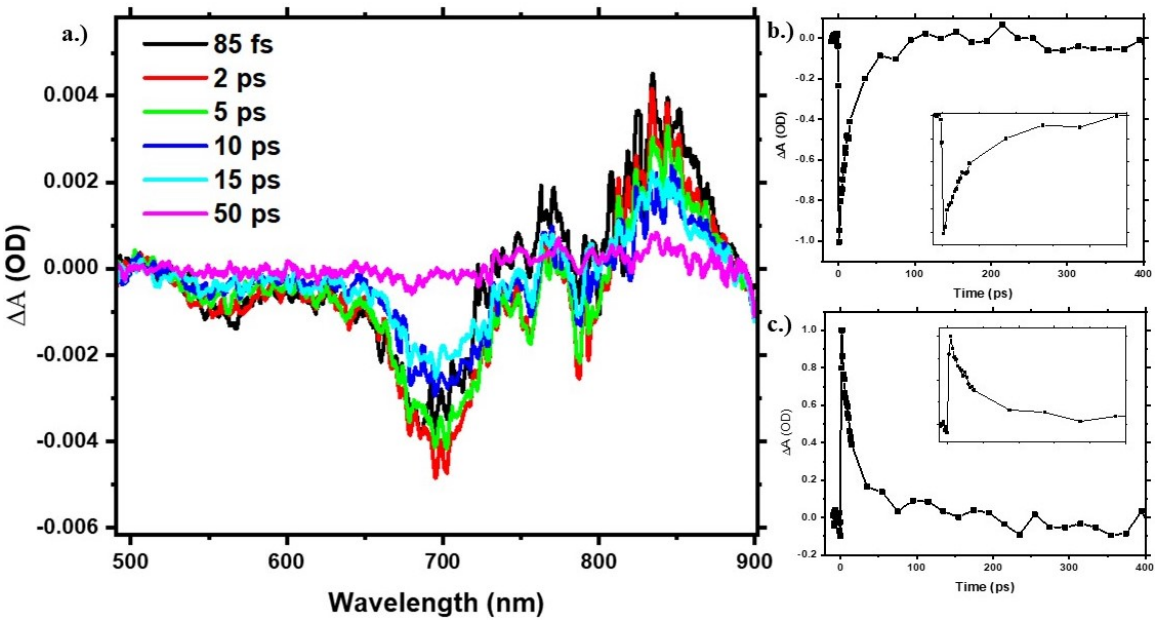

Figure 3.8. Transient absorption spectra for fiber 1, at various time delays, with pump wavelength at 400 nm. b) kinetics at 700 nm (GSB), the inset shows the kinetics for the first 100 ps. c) kinetics at 850 nm (PIA), the inset shows kientics for first 100 ps.

TAS is also conducted on fiber 2, as shown in Figure 3.9 with pump wavelength at 540 nm. At this pump wavelength, only a GSB signal is observed, positioned at *ca.* 650 nm. The inset of Figure 3.9 shows the corresponding kinetics at 650 nm, for the first 100 ps. Similar to fiber 1, the kinetics of the GSB signal nearly completely deplete within the first *ca.* 100 ps. It is important to note that probing at this longer wavelength does not promote the excited state population to another state, thus there is no observed PIA signal.

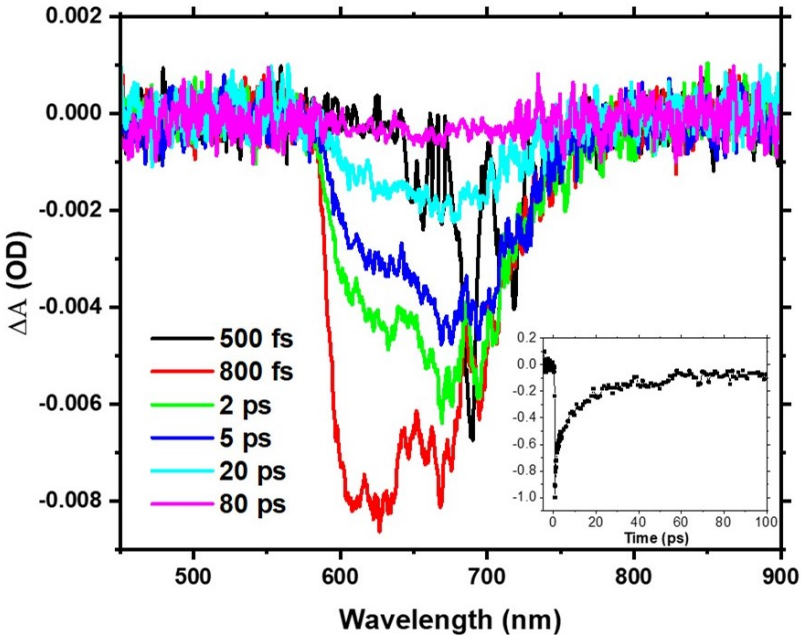

Figure 3.9. Transient absorption spectra for fiber 2, at various time delays, with pump 540 nm. The inset shows the kinetics at 620 nm for the first 100 ps.

3.3.5 Conclusion

In conclusion, we study the optical anisotropy of a simple and scalable method to produce polymer microfibers pulled from a melt solution of DPP-C5. These fibers exhibit a high degree of ordering within domains along the fiber. The anisotropy observed in the polarized PL, TR-PL and PL images suggests that TDMs of the

polymer chains (in the direction of the polymer backbone) pack along the short axis of the fiber. The polarized PL display a maximum PL intensity when exciting along the polymer short axis ($\perp$ excitation), as well as collecting emission along the polymer short axis ($\perp$ detection). As the TDM corresponds to the direction in which electronic transitions from one state to another state occurs, the maximum PL intensity observed for the ($\perp$, $\perp$) direction suggests that the maximum absorbance, and consequently emission, occurs in this direction.

From the polarized TR-PL, it is difficult to observe an obvious dependence of excited state lifetimes with polarization direction, as this technique only measures radiative pathways. This is due to the nature of radiative recombination pathways; many different radiative pathways may correspond to one lifetime, and so it is difficult to discern different pathways based only on the measured radiative lifetime. Generally, the TR-PL lifetimes show that there are two lifetimes in the excited state decays, one shorter lifetime, (τ_1, *ca.* 60 ps) and one longer lifetime (τ_2, *ca.* 200 ps). We do observe in one domain the perpendicular excitation, perpendicular detection ($\perp$, $\perp$) and parallel excitation, perpendicular detection ($\parallel$, $\perp$) yields longer lifetimes, suggesting a FRET mechanism which lengthens the exciton lifetime.

TAS, a technique which probes non-radiative pathways, is conducted on both fiber 1 and 2, with pump wavelengths of 400 nm and 540 nm, respectively. In both fibers, the GSB signals decay within the first *ca.* 100 ps. When probing fiber 1 with pump with wavelength of 400 nm, a GSB at 700 nm, and PIA, a 850 nm, are observed. Both signals decay significantly within the first 100 ps. Fiber 2, pumped with 540 nm, does not exhibit a PIA, likely due to the longer wavelength pump, providing insufficient energy to promote the excited state to a higher state. Furthermore, with this pump wavelength, the GSB is centered at 620 nm, blue shifted from the pump 400 nm GSB centered at 700 nm.

4. EXCITON DIFFUSION IN ALIGNED POLYMER CHAINS BY SOLUTION COATING

4.1 Introduction

A major advantage of semiconducting polymers is their compatibility with low-cost and high-throughput fabrication methods, such as roll-to-roll processing. Solution printing of OPVs offers simple, large-scale production however, controlling the film morphology largely remains a challenge. Recent work has demonstrated control over bulk and surface morphologies by implementing a solution coating technique [33], [34], [35]. Varying the temperature of the polymer solution, coating speed and printing direction changes the arrangement of polymer chains within the film. This technique allows for control in ordering molecular aggregates relative to the substrate.

Ensemble measurements of these films exhibit high degrees of optical anisotropy, however an understanding of exciton diffusion as a function of printing parameters has yet to be established [33]. Herein, we study how altering the printing rate and concentration of polymer solutions changes the packing morphology and consequently exciton diffusion.

4.2 Sample Preparation

PII-2T solutions (structure shown in Figure 4.1) of varying concentrations are prepared. Solution coating of films is prepared by shearing the polymer solution along a quartz substrate at a continuous flow rate. Detailed procedures are provided elsewhere [33], [34], [35]. Three different samples with various solution concentrations

and flow rates are analyzed. Samples 1, 2 and 3 are prepared as follows: sample 1 is coated from a 10 mg/mL solution at a flow rate of 0.25 mm/s; sample 2 is coated from a 30 mg/mL solution at a rate of 1 mm/s; sample 3 is coated from a 30 mg/mL solution at 5mm/s.

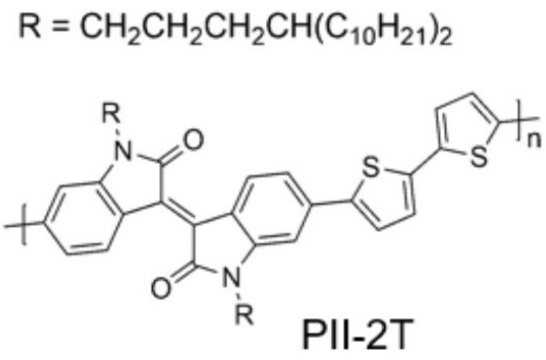

Figure 4.1. Molecular structure of PII-2T polymer utilized in sheared thin films.

4.3 Results and Discussion

4.3.1 Sample Characterization

Absorption spectra of the coated films are provided in Figure 4.2, where the incident beam is polarized either parallel or perpendicular to the printing direction. The relative absorption is largest when the incident light is parallel to the printing direction, which is in agreement with polymer backbones lying in the printing direction [33]. Furthermore, it is observed that varying the printing speed impacts the anisotropy of absorption spectra significantly; sample 2, printed at 1 mm/s, yields a stark contrast in parallel and perpendicular absorption signals, suggesting a higher extent of ordering. Sample 1, which is printed at 0.25 mm/s, does not exhibit a large difference in perpendicular and parallel absorption signals, suggesting that polymer chains are less ordered.

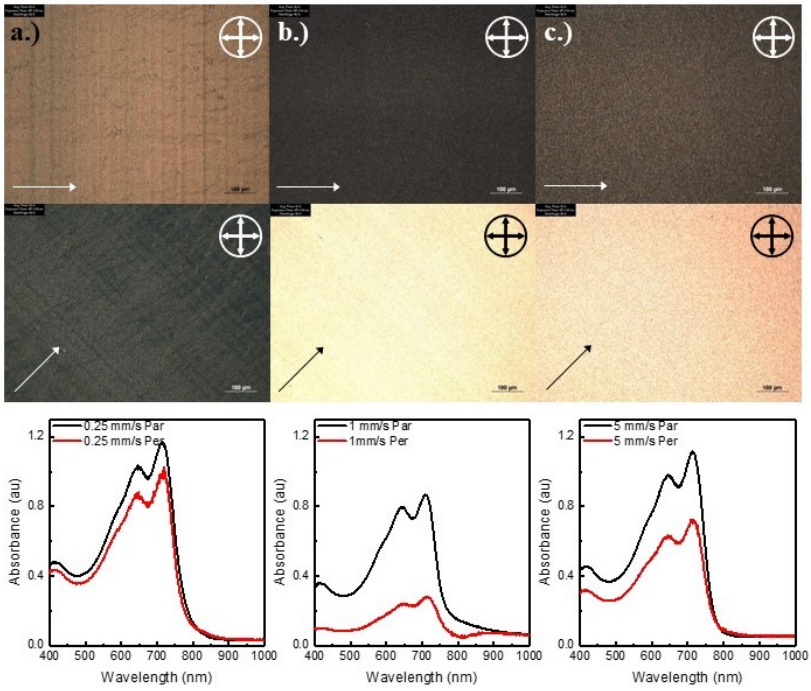

Figure 4.2. Cross-polarized optical microscopy images (c-POM) for sheared films a) 1 b) 2 and c) 3. The white arrow indicates printing direction and the cross-hairs show the direction of cross-polarization.

Figure 4.2 also includes cross-polarized optical microscope images (c-POM) of the films, with the cross polarization direction indicated in the top-left, and the printing direction indicated by the arrow in the bottom-left. For samples 2 and 3, total light extinction is observed when the printing direction aligns with the cross-polarization direction. As the TDM of PII-2T runs along the backbone of the polymer, the c-POM images correspond to polymer chains aligning in the printing direction. In sample 1 however, total light extinction occurs when the sample is rotated 45° from one polarization axis. This suggests no preferential orientation of polymer chains with the printing direction, as observed by the bright c-POM image obtained which is in good agreement with the polarized absorption spectra.

4.3.2 Polarized PL and TR-PL

Polarized PL is conducted on samples 1, 2 and 3 to elucidate any polarization dependencies that may arise from varying printing parameters (i.e. flow rate and concentration). Figure 4.3 shows the PL intensities corresponding to various polarization directions for samples a) 1 b) 2 and c) 3. Here the notation ($\perp$ $\perp$, $\parallel$ $\perp$, etc.) again correspond to the excitation and detection direction, respectively, along the printing direction. It has been demonstrated that polymer chains align in the printing direction within the surface layer, however the bulk morphology is not as well controlled and as a result is more amorphous. As a result, the polarized PL does not reflect any consistent trends in maximum polarized PL intensity with printing direction.

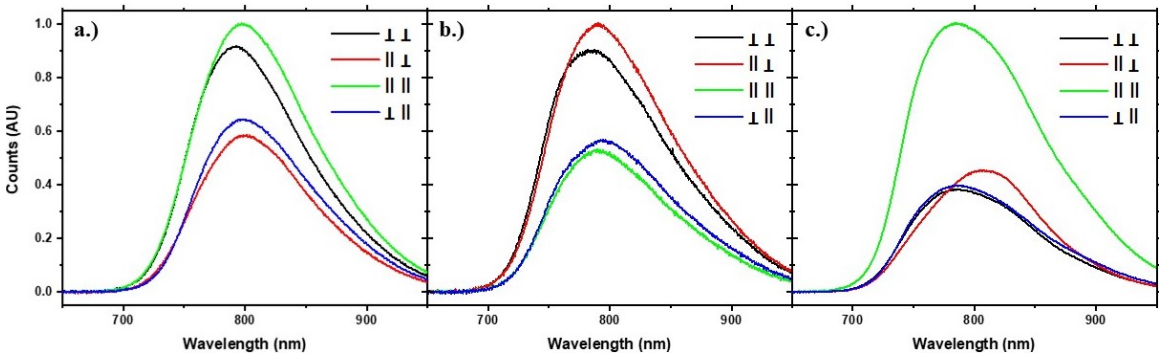

Figure 4.3. Polarized PL spectra for samples a) 1 b) 2 c) 3 normalized to the maximum intensity. Perpendicular and parallel notation corresponds to excitation, detection direction along the printing direction. Due t to the amorphous morphology within the bulk of the film, there is no observed polarization dependence in PL intensities.

Power-dependent TR-PL is also conducted on the films, to again ensure there are no additional processes occurring such as exciton-exciton annihilation. A variety of pump fluences are employed on all samples, as shown in Figure 4.4. The excited state

lifetimes, for various pump powers, do not change significantly among the films which indicates that there is no power dependence.

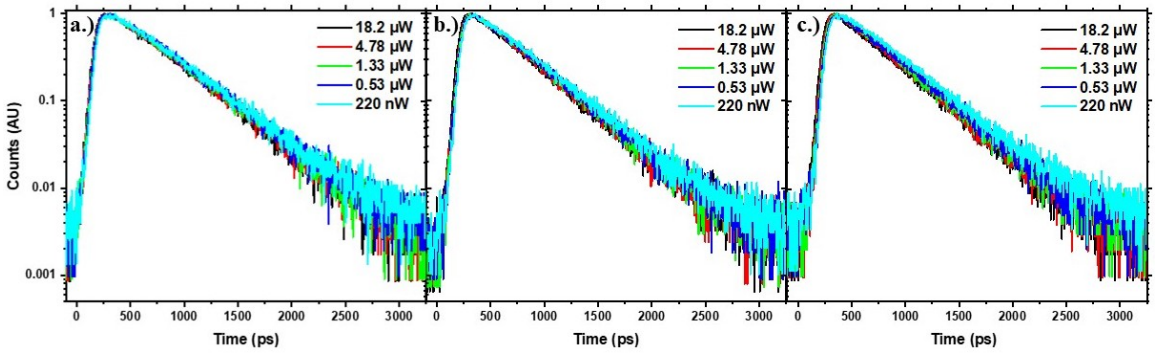

Figure 4.4. Power-dependent TR-PL excited state lifetimes for samples a) 1 b) 2 and c) 3. Changing pump power does not significantly change excited state lifetimes in any of the films, demonstrating that films do not exhibit a power dependence.

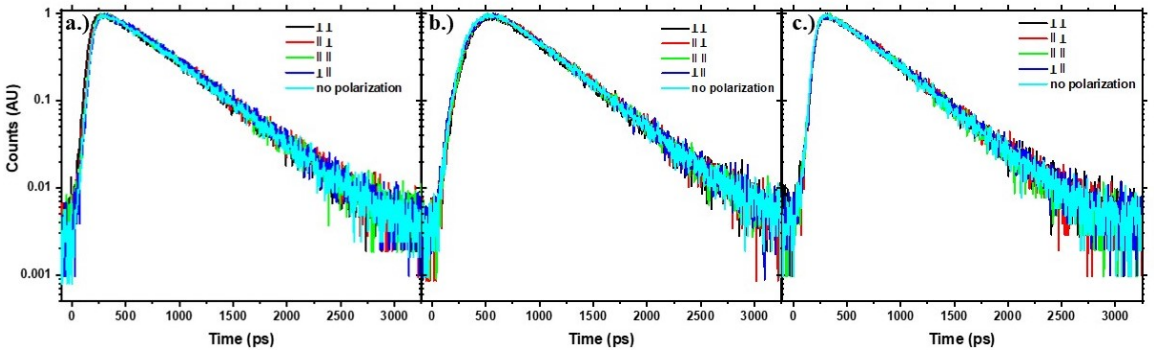

Figure 4.5. Polarized TR-PL for samples a) 1 b) 2 and c) 3.

Polarized TR-PL is also conducted on samples, 1, 2, and 3, provided in Figure 4.5. In agreement with the polarized PL, excited state lifetimes do not exhibit any polarization dependence. As TR-PL only probes radiative recombination pathways,

the amorphous material within the bulk of the film results in no observed polarization dependencies. From the TR-PL data of sample 2 (Figure 4.5 b), a rise time is observed in the first 500 ps, for all polarization directions. Table 4.1 provides lifetimes for all polarization directions in all three samples, demonstrating no changes in τ_1 or τ_2 between polarization directions or without polarizing the excitation or detection direction.

Table 4.1.
Polarized Excited State lifetimes for Sheared Samples 1, 2 and 3.

Sample	Excitation	Detection	τ_1 (ps)	τ_1 (ps)
1	$\parallel$	$\parallel$	195	446
	$\parallel$	$\perp$	193	451
	$\perp$	$\perp$	164	457
	$\perp$	$\parallel$	222	442
	N/A	N/A	142	461
2	$\parallel$	$\parallel$	112	442
	$\parallel$	$\perp$	126	438
	$\perp$	$\perp$	147	436
	$\perp$	$\parallel$	99	447
	N/A	N/A	133	436
3	$\parallel$	$\parallel$	151	423
	$\parallel$	$\perp$	174	427
	$\perp$	$\perp$	157	427
	$\perp$	$\parallel$	188	419
	N/A	N/A	177	422

Polarized PL images of the sheared films are also collected, shown in Figure 4.6. PL emission from the samples does not change when changing polarization direction, as the relative PL intensities and distributions remain consistent among polarization

configurations. Furthermore, the samples exhibit inhomogeneity throughout the surface, displaying a higher PL emission on one side of the measured area. When no polarization is introduced to the sample (Figure 4.6 e) the film appears to be highly ordered, observed by the linear pattern in the PL image. These images confirm that due to the amorphous nature of the films, as well as their inhomogeneity, there is no observable polarization dependence.

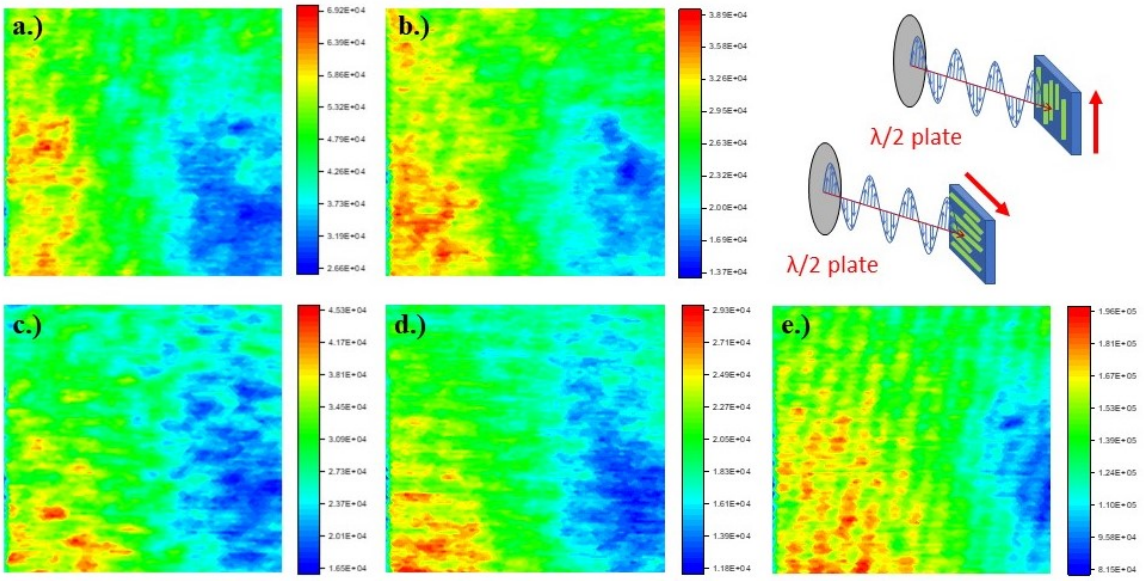

Figure 4.6. Polarized PL images of sheared sample 1, with polarization directions a) ∥ excitation, ∥ detection b) ⊥ excitation, ∥ detection c) ⊥ excitation, ⊥ detection d) ∥ excitation, ⊥ detection and e) no polarization. A schematic representation of the excitation polarization, relative to the sample, is included as well. The red arrow indicates sample printing direction.

4.3.3 Transient Absorption Spectroscopy

TAS for all three solution-coated samples is obtained for pump wavelengths 700 nm as well as 650 nm. Figure 4.7 displays the TAS spectra for sample 1, with two different pump wavelengths, a) 700 nm and b) 650 nm. Corresponding kinetics are

provided at 720 nm, for the first 250 ps. In both spectra, it is observed that the GSB signal nearly completely depletes after 200 ps. Furthermore, with a pump wavelength of 700 nm, there is a very fast component within the first < 20 ps, in which the signal intensity is nearly halved.

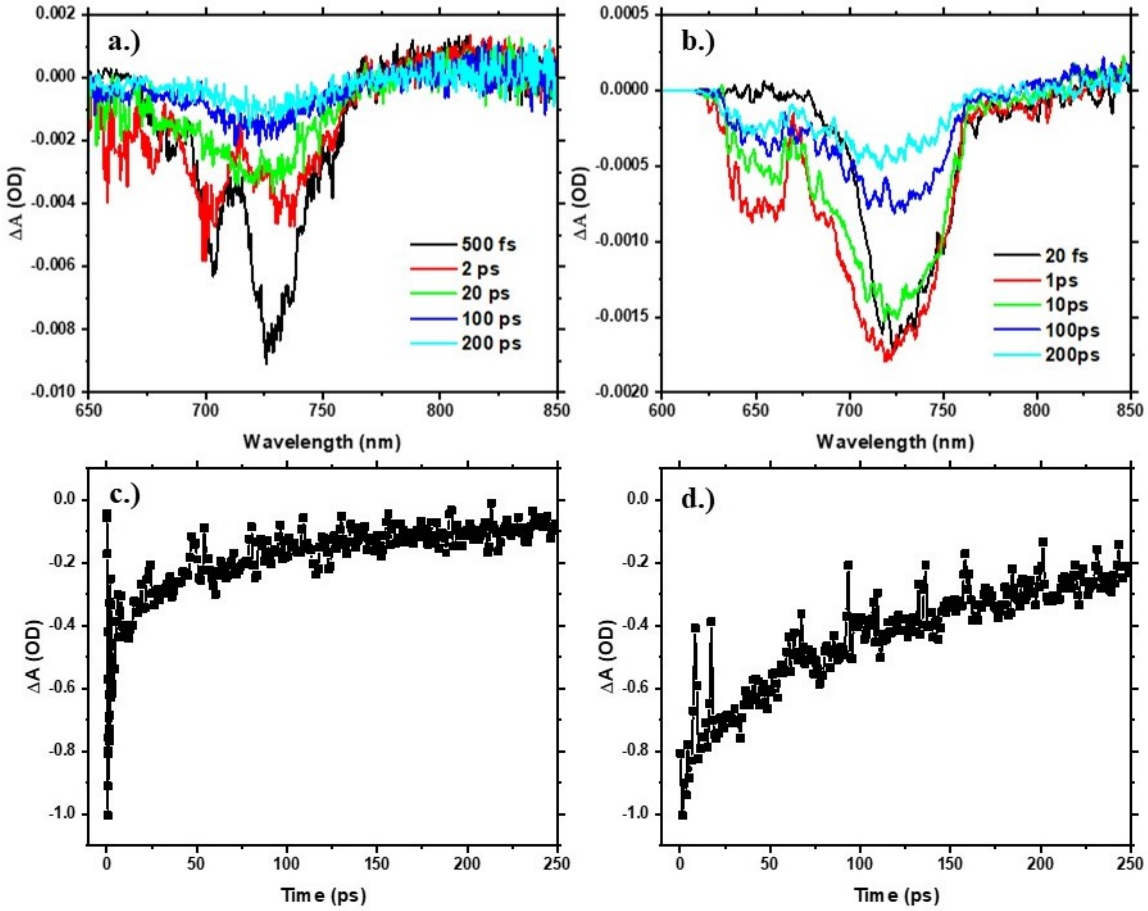

Figure 4.7. TAS spectra for sample 1 with pump wavelengths a) 700 nm and b) 650 nm. Corresponding kinetics at 720 nm are given for pump c) 700 nm and d) 650 nm.

It is observed in Figure 4.8 that the transient absorption kinetics of sample 2 do not exhibit any pump wavelength dependencies. Figure 4.8 a) and b) show the TA spectra for pump 700 nm and 650 nm, with their corresponding kinetics given in b)

and d), respectively. Despite the variation in pump wavelengths, the ΔA signals in both spectra decrease at similar rates.

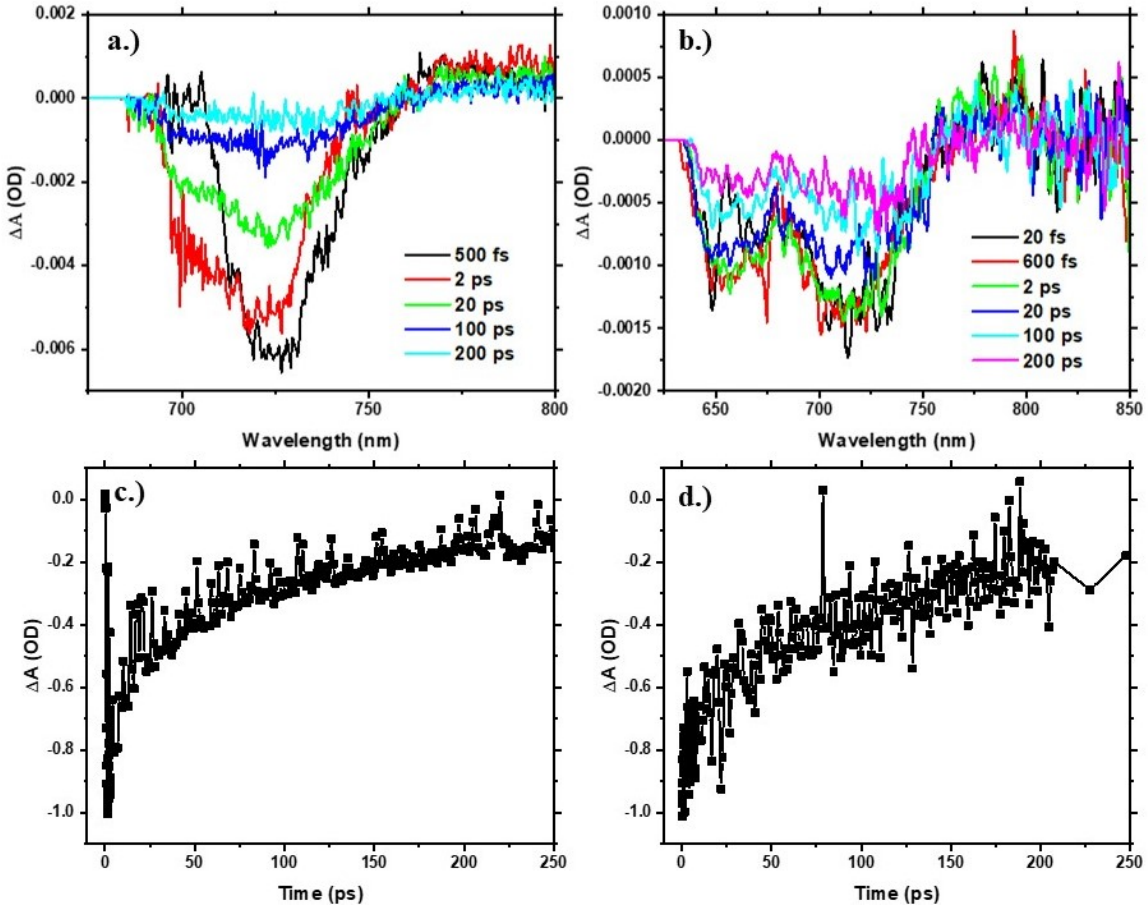

Figure 4.8. TAS spectra for sample 2 with pump wavelengths a) 700 nm and b) 650 nm. Corresponding kinetics at 720 nm are given for pump c) 700 nm and d) 650 nm.

As shown in Figure 4.9, sample 3 exhibits a pump wavelength dependence. Figure 4.9 displays the TAS spectra for sample 3, with a) 700 nm and b) 650 nm pump wavelengths and their corresponding kinetics, c) and d), respectively. Utilizing pump 700 nm causes an initial fast component in the ΔA signal, as seen within the first ∼20 ps in Figure 4.9 c.

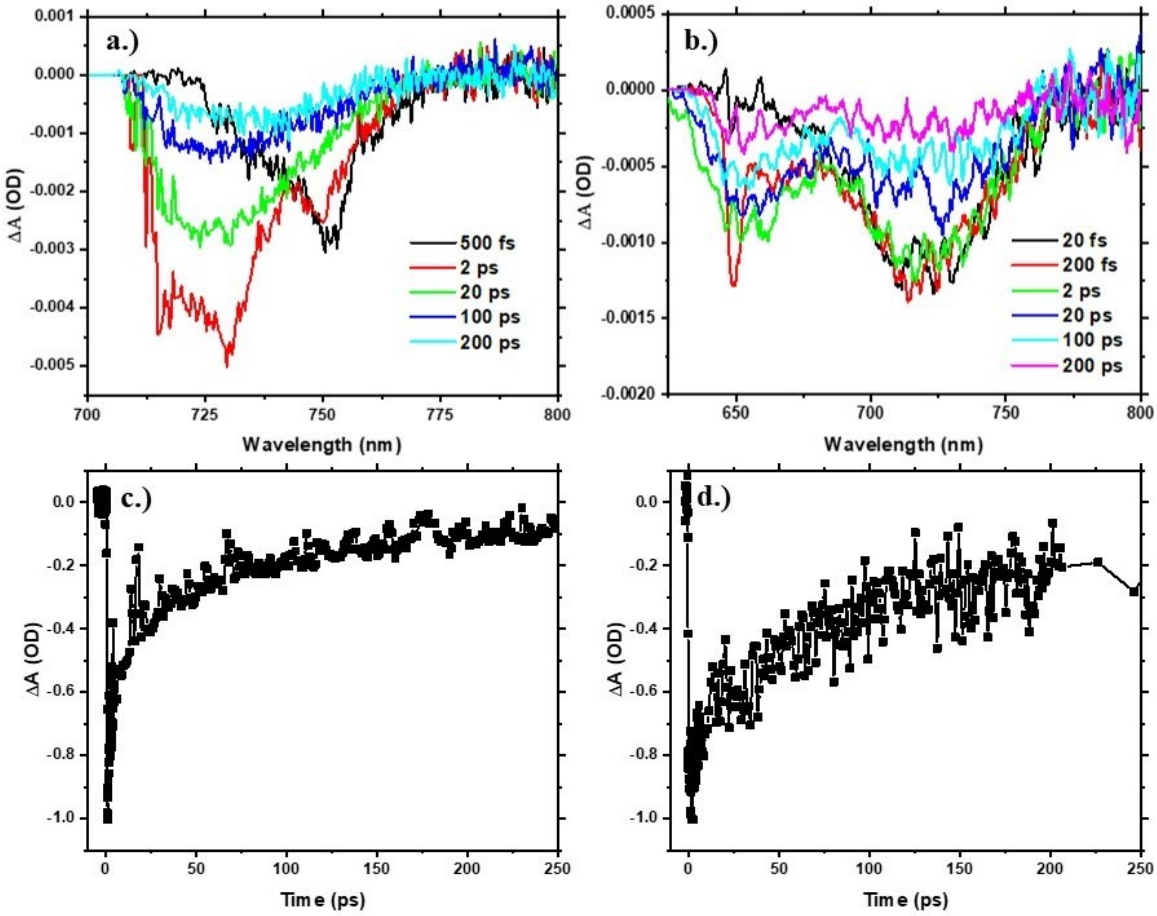

Figure 4.9. TAS spectra for sample 3 with pump wavelengths a) 700 nm and b) 650 nm. Corresponding kinetics at 720 nm are given for pump c) 700 nm and d) 650 nm.

4.3.4 Transient Absorption Microscopy

From the white light probe source incorporated in TAS analysis, the optimal wavelength to probe for transient absorption microscopy (TAM) is extracted. The GSB signals are generally located at 720 nm, for both 700 nm and 650 nm pump wavelengths. As a result, TAM is conducted using a pump wavelength of 690 nm and probe wavelength of 720 nm on the film samples. Diffusion images for sample 1, 2

and 3 are provided in Figures 4.10, 4.12 and 4.14, respectively, at a number of time delays. From these images, it is observed that carrier diffusion occurs symmetrically, such that diffusion rates are similar in all directions. From these images, the exciton diffusion profiles are extracted.

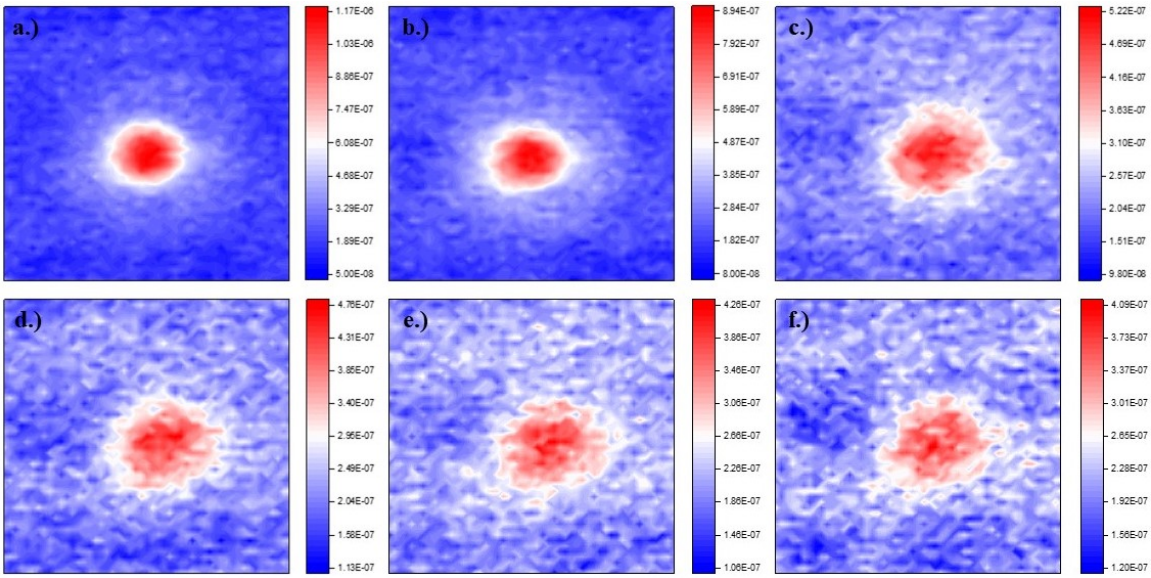

Figure 4.10. TAM images of sample 1 with pump 690 nm and probe 700 nm, for the following delay times: a) 0 ps b) 10 ps c) 40 ps d) 60 ps e) 80 ps f) 100 ps. Scale bar shows ΔA intensity

Figure 4.11 a provides the diffusion profiles extracted from the TAM images for sample 1, as well as the TA dynamics with pump 690 nm and probe 720, Figure 4.11 b. Though decaying, the signal is still observed within the first 100 ps. Fitting the Gaussian profiles to extract the variance, $\sigma^2{}_x(t)$, and plotting these at each time delay provides the plot in Figure 4.11 c. Fitting this plot with a linear regression and extracting the slope, we are able to determine the diffusion constant, D_x [36]. For sample 1, D_x= ∼9.15 cm^2/s. Sample 1 is coated at the slowest rate, 0.25mm/s, with the lowest concentration, 10 mg/mL, which yields a slower diffusion constant. Additionally, sample 1 has no observable optical anisotropy in the polarized absorbance

spectra, further suggesting no preferred orientation of polymer chains. As a result, this hinders exciton diffusion in the film, as it is too disordered to form a sufficiently delocalied network.

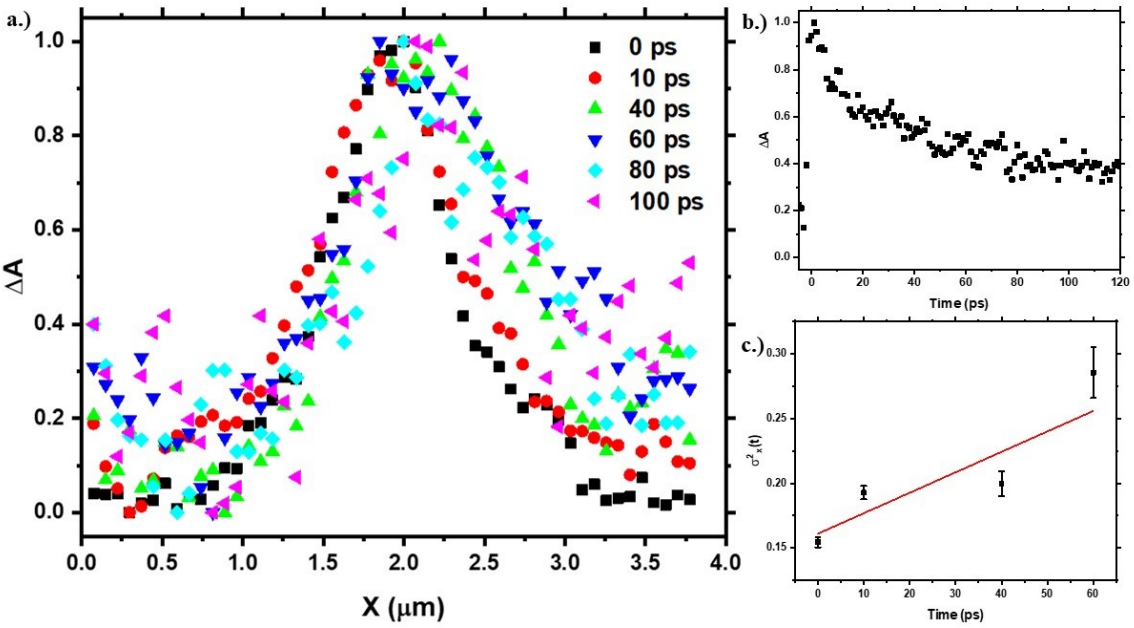

Figure 4.11. TAM for sample 1: a) diffusion profiles extracted from the TAM images b) kinetics for pump 690 nm, probe 720 nm c)

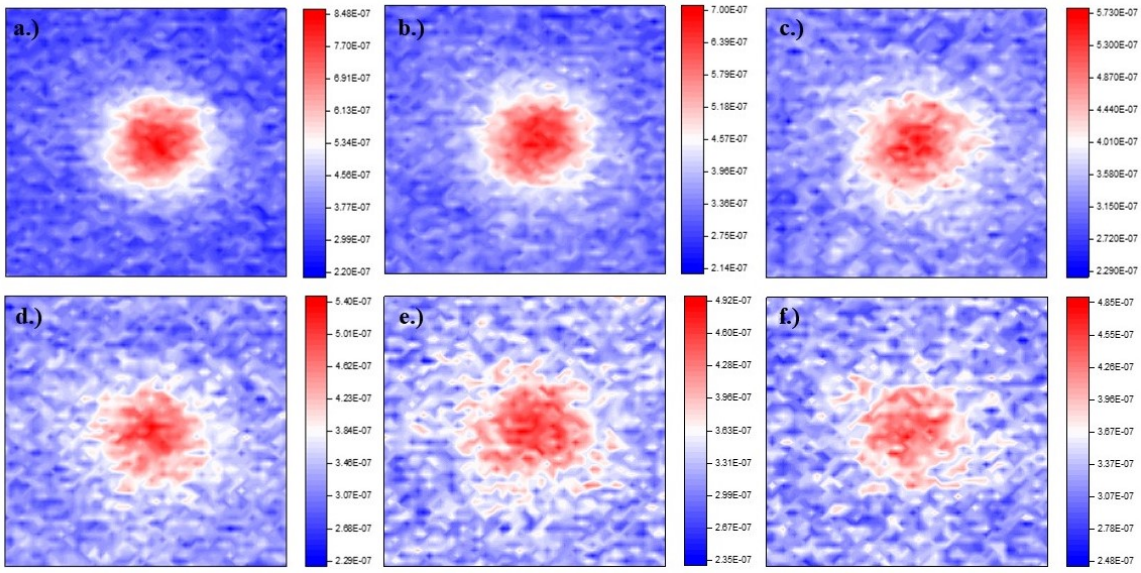

Figure 4.12. TAM images of sample 2 with pump 690 nm and probe 700 nm, for the following delay times: a) 0 ps b) 20 ps c) 40 ps d) 60 ps e) 80 ps f) 100 ps. Scale bar shows ΔA intensity

Figure 4.13 a provides the diffusion profiles extracted from the TAM images for sample 2, as well as the TA dynamics for the first 120 ps in Figure 4.13 b. Fitting the extracted Gaussian profiles and using the slope, the diffusion constant is determined as $D_x = \sim 13.9$ cm^2/s. The larger diffusion constant is in good agreement with the optical ansitropy, which suggests a greater extent of ordering within the film. Ordering of the polymer chains allows for stronger electronic coupling between aggregates, enabling a slightly faster exciton diffusion rate.

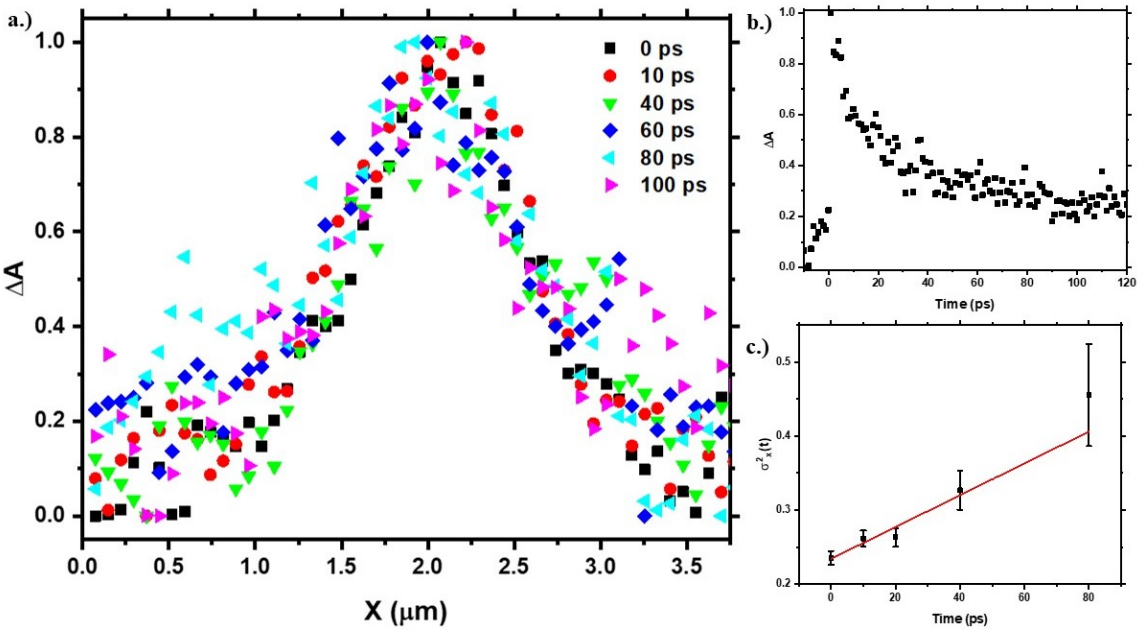

Figure 4.13. TAM for sample 2: a) diffusion profiles extracted from the TAM images b) kinetics for pump 690 nm, probe 720 nm c)

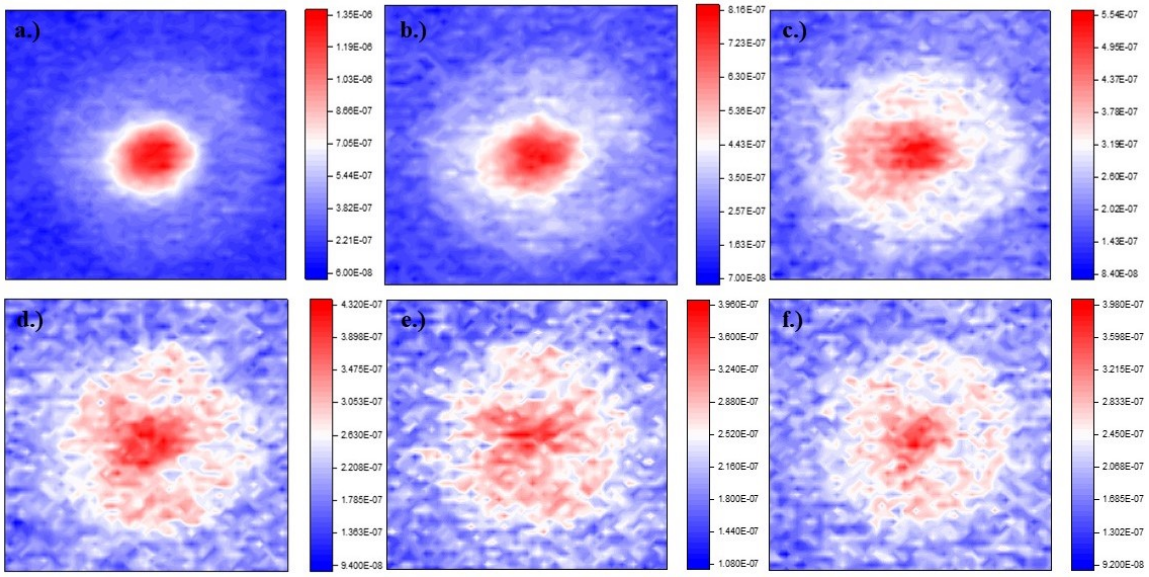

Figure 4.14. TAM images of sample 3 with pump 690 nm and probe 700 nm, for the following delay times: a) 0 ps b) 10 ps c) 40 ps d) 60 ps e) 80 ps f) 100 ps. Scale bar shows ΔA intensity

Figure 4.15 a provides the diffusion profiles extracted from the TAM images for sample 3, and TA dynamics as well, also for the first 120 ps as seen in Figure 4.13 b. From the Gaussian profiles, the diffusion constant is determined as D_x= ∼33.5 cm^2/s. Sample 3 yields the largest diffusion, and is coated at the fastest deposition rate, 5mm/s. It appears that these printing parameters form a network of well-ordered polymer chains with delocalization, which allow for larger exciton diffusion constants.

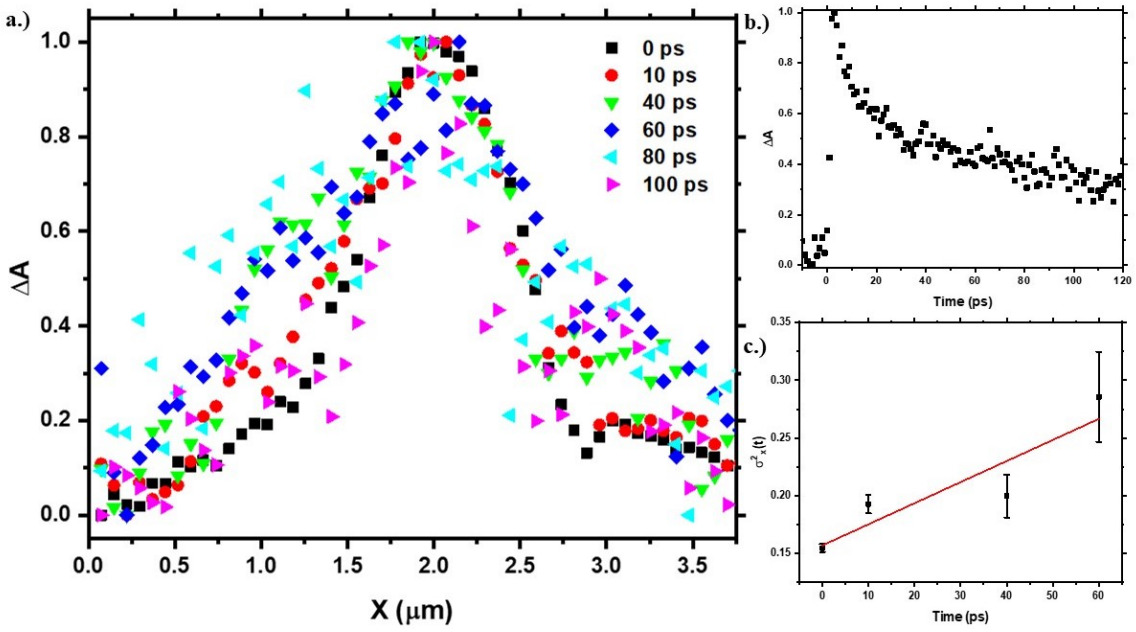

Figure 4.15. TAM for sample 3: a) diffusion profiles extracted from the TAM images b) kinetics for pump 690 nm, probe 720 nm c)

4.4 Conclusion

In conclusion, we systematically study exciton transport in polymer films with varying deposition parameters. Films are shear-coated, with differing concentrations as well as shearing speeds which dictates the morphology of the polymer chain alignment. As a result, the bulk optical properties of the films exhibit ansiotropy, as seen in the c-POM images and absorbance spectra. This suggests that depending upon the deposition parameters, polymer chains adapt a preferential packing orientation. However, the polarized PL spectra do not exhibit anisotropy, mainly due to the inhomogeniety of the films.

From the TAS, the pump and probe wavelengths are obtained for TAM, which is conducted with pump 690 nm and probe 720 nm. From the TAM images, it is observed that the exciton diffusion is symmetric in both x and y. Extracting the variance from

the Gaussian profiles and plotting these at various time delays provides $2D_{2}$. We determine that there is a strong dependence of diffusion constant on the deposition parameters. Sample 1, which is coated from a 10mg/mL solution at 25mm/s, has the slowest diffusion constant of $\sim$9.15 cm^2/s. Sample 2 is coated at 1mm/s from a 30mg/mL solution and has a diffusion constant of $\sim$13.9 cm^2/s. Lastly, sample 3, coated from 30 mg/mL solution at 5 mm/s has a diffusion constant of $\sim$33.5 cm^2/s.

Although all films are well-ordered and exhibit optical anisotorpy, our results demonstrate that to achieve long exciton diffusion lengths careful consideration must be given in deposition parameters. We found that this simple and scalable film fabrication technique enables diffusive excitons, capable of migrating long-ranges. Based on these preliminary results, it is apparent that desired long-range exciton diffusion lengths can be achieved through coherence by tuning polymer chain orientations. Further TAM studies, to exploit diffusion constants for differing deposition parameters, will be conducted to understand how polymer thin film morphologies influence exciton dynamics and transport.

REFERENCES

[1] Allen McFarland. In 2018 the united states consumed more energy than ever before. *U.S. Energy Information Administration*, 2019.

[2] IEA. Global energy and co_2 status report. *International Energy Agency*, 2019.

[3] Emission Database for Global Atmospheric Research (EDGAR). Global energy and co_2 status report. *International Energy Agency*, 2019.

[4] William Shockley and Hans J. Queisser. Detailed blanace limit efficiency of p-n junction solar cells. *J. Appl. Phys.*, 32:510–519, 1961.

[5] Michael Woodhouse, Brittany Smith, Ashwin Ramdas, and Robert Margolis. Crystalline silicon photovoltaic module manufacturing costs and sustainable pricing: 1h 2018 benchmark and cost reduction roadmap. *National Renewable Energy Laboratory*, 2019.

[6] Bernard Kippelen and Jean-Luc Bredas. Organic photovoltaics. *Energy Environ. Sci.*, 2:251–261, 2009.

[7] T. Aernouts, T. Aleksandrov, C. Girotto, J. Genoe, and J. Poortmans. Polymer based organic solar cells using ink-jet printed active layers. *Appl. Phys. Lett.*, 92:03306, 2008.

[8] Artem A. Bakulin, Akshay Rao, Vlad G. Pavelyev, Paul H. M. van Loosdrecht, Maxim S. Pshenichnikov, Dorota Niedzialek, Jérôme Cornil, David Beljonne, and Richard H. Friend. The role of driving energy and delocalized states for charge separation in organic semiconductors. *Science*, 335:1340–1344, 2012.

[9] Harald Hoppe and Niyazi Sariciftci. Morphology of polymer/fullerene bulk heterojunction solar cells. *Journal of Materials Chemistry*, 16:45–61, 2006.

[10] Christoph Brabec, Srinivas Gowrisanker, Jonathan Halls, Darin Laird, and Shijun Jia. Polymer-fullerene bulk-heterojunction solar cells. *Advanced Materials*, 22:3839–3856, 2010.

[11] Jean-Luc Bredas, Joseph E. Norton, Jerome Cornil, and Veaceslav Coropceanu. Molecular understanding of organic solar cells: The challenges. *Accouns of Chemical Resarch*, 42:1691–1699, 2009.

[12] Xiaoyang Zhu, Nicholas R. Monahan, Zizhou Gong, Haiming Zhu, Kristopher W. Williams, and Cory A. Nelson. Charge transfer excitons at van der waals interfaces. *J. Am. Chem. Soc*, 137:8313–8320, 2015.

[13] B. Bernardo, D. Cheyns, B. Verreet, R.D. Schaller, B.P. Rand, and N.C. Giebink. Delocalization and dielectric screening of charge transfer states in organic photovoltaic cells. *Nature Communication*, 5:3245, 2014.

[14] Xu-Hui Jin, Michael B. Price, John R. Finnegan1, Charlotte E. Boott1, Johannes M. Richter, Akshay Rao, S. Matthew Menke, Richard H. Friend, George R. Whittell, and Ian Manners. Long-range exciton transport in conjugated polymer nanofibers prepared by seeded growth. *Science*, 360:897–900, 2018.

[15] A. S. Davydov. Theory of molecular excitons. *Springer*, 1971.

[16] T. Förster. Zwischenmolekulare energiewanderung und fluoreszenz. *Annalen der Physik*, 437:55–75, 1948.

[17] D. L. Dexter. A theory of sensitized luminescence in solids. *J. Chem. Phys.*, 21:836, 1953.

[18] D. Beljonne, G. Pourtois, C. Silva, E. Hennebicq, L. M. Herz, R. H. Friend, G. D. Scholes, S. Setayesh, K.Mullen, and J. L. Bredas. Interchain vs. intrachain energy transfer in acceptor capped conjugated polymers. *PNAS*, 99:10982–10987, 2002.

[19] Jean-Luc Bredas, Edward H. Sargent, and Gregory D. Scholes. Photovoltaic concepts inspired by coherence effects in photosynthetic systems. *Nature Materials*, 16:35–44, 2017.

[20] Joonsuk Huh, Semion K. Saikin, Jennifer C. Brookes, Stéphanie Valleau, Takatoshi Fujita, and Alán Aspuru-Guzik. Atomistic study of energy funneling in the light-harvesting complex of green sulfur bacteria. *J. Am. Chem. Soc.*, 136:2048–2057, 2014.

[21] A. Chenu and G. D. Scholes. Coherence in energy transfer and photosynthesis. *Annu. Rev. Phys. Chem.*, 66:69–96, 2015.

[22] E. A. Codling, M. J. Plank, and S. Benhamou. Random walk models in biology. *J. R. Soc. Interface*, 25:813–834, 2008.

[23] Elisabetta Collini and Gregory D. Scholes. Coherent intrachain energy migration in a conjugated polymer at room temperature. *Science*, 323:369, 2009.

[24] Zheng-Ming Huanga, Y.-Z. Zhangb, M. Kotakic, and S. Ramakrishnab. A review on polymer nanofibers by electrospinning and their applications in nanocomposites. *Composites Science and Technology*, 63:2223–2253, 2003.

[25] Suhao Wang, Michael Kappl, Ingo Liebewirth, Maren Müller, Katrin Kirchhoff, Wojciech Pisula, and Klaus Müllen. Organic field-effect transistors based on highly ordered single polymer fibers. *ADv. Mater.*, 24:417–420, 2012.

[26] Sungwon Lee, Geon Dae Moona, and Unyong Jeong. Continuous production of uniform poly(3-hexylthiophene) (p3ht) nanofibers by electrospinning and their electrical properties. *J. Mater. Chem*, 19:743–748, 2009.

[27] Eleonora V. Canes, Alessandro Luzio, Beatrice Saglio, Andrea Bianco, Mario Caironi, and Chiara Bertarelli. n-type semiconducting polymer fibers. *ACS Macro. Lett.*, 3:366–369, 2012.

[28] Xikang Zhao, Guobiao Xue, Ge Qu, Vani Singhania, Yan Zhao, Kamal Butrouna, Aristide Gumyusenge, Ying Diao, Kenneth R. Graham, Hanying Li, and Jianguo Mei. Complementary semiconducting polymer blends: Influence of side chains of matrix polymers. *Macromolecules*, 50:6202–6209, 2017.

[29] Xikang Zhao, Yan Zhao, Qu Ge, Kamal Butrouna, Ying Diao, Kenneth R. Graham, and Jianguo Mei. Complementary semiconducting polymer blends: The influence of conjugation-break spacer length in matrix polymers. *Macromolecules*, 49:2601–2608, 2016.

[30] Yan Zhao, Aristide Gumyusenge, Jiazhi He, Ge Qu, William W. McNutt, Yuan Long, Hongyi Zhang, Libai Huang, Ying Diao, and Jianguo Mei. Continuous melt-drawing of highly aligned flexible and stretchable semiconducting microfibers for organic electronics. *Adv. Funct. Mater.*, 28:1705584, 2018.

[31] Dean M. DeLongchamp, R. Joseph Kline, Youngsuk Jung, David S. Germack, Eric K. Lin, Andrew J. Moad, Lee J. Richter, Michael F. Toney, Martin Heeney, and Iain McCulloch. Controlling the orientation of terraced nanoscale "ribbons" of a poly(thiophene) semiconductor. *ACS Nano*, 3:780–787, 2009.

[32] Volkhard May. Kinetic theory of exciton-exciton annihilation. *J. Chem. Phys.*, 140:054103, 2009.

[33] Ge Qu, Xikang Zhao, Gregory M. Newbloom, Fengjiao Zhang, Erfan Mohammadi, Joseph W. Strzalka, Lilo D. Pozzo, Jianguo Mei, and Ying Diao. Understanding interfacial alignment in solution coated conjugated polymer thin films. *ACS Appl. Mater. Interfaces*, 9:27863–27874, 2017.

[34] Erfan Mohammadi, Chuankai Zhao, Yifei Meng, Ge Qu, Fengjiao Zhang, Xikang Zhao, Jianguo Mei, Jian-Min Zuo, Diwakar Shukla, and Ying Diao. Dynamic-template-directed multiscale assembly for large-area coating of highly-aligned conjugated polymer thin films. *Nature Communications*, 8:16070, 2017.

[35] Fengjiao Zhang, Erfan Mohammadi, Xuyi Luo, Joseph Strzalka, Jianguo Mei, and Ying Diao. Critical role of surface energy in guiding crystallization of solution-coated conjugated polymer thin films. *Langmuir*, 34:1109–1122, 2018.

[36] Zhi Guo, Joseph S. Manser, Yan Wan, Prashant V. Kamat, and Libai Huang. Spatial and temporal imaging of long-range charge transport in perovskite thin films by ultrafast microscopy. *Nature Communcation*, 6:7471, 2015.